

AD-A194 836	DYNAMIC FRACTURE TOUGHNESS EVALUATION BY MEASUREMENT OF CTD0 (CRACK TIP 0.) (U) JOHNS HOPKINS UNIV BALTIMORE MD DEPT OF MECHANICAL ENGINEERIN.. W N SHARPE ET AL.	1/1
UNCLASSIFIED	15 MAR 88 MMS/ASD-88-82 ARO-22684. 2-EG	F/G 11/6.1 NL

AD-A194 836	DYNAMIC FRACTURE TOUGHNESS EVALUATION BY MEASUREMENT OF CTD0 (CRACK TIP 0.) (U) JOHNS HOPKINS UNIV BALTIMORE MD DEPT OF MECHANICAL ENGINEERIN.. W N SHARPE ET AL.	1/1
UNCLASSIFIED	15 MAR 88 MMS/ASD-88-82 ARO-22684. 2-EG	F/G 11/6.1 NL

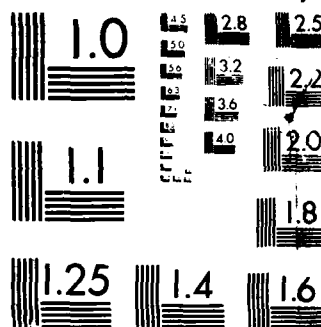
AD-A194 836	DYNAMIC FRACTURE TOUGHNESS EVALUATION BY MEASUREMENT OF CTD0 (CRACK TIP 0.) (U) JOHNS HOPKINS UNIV BALTIMORE MD DEPT OF MECHANICAL ENGINEERIN.. W N SHARPE ET AL.	1/1
UNCLASSIFIED	15 MAR 88 MMS/ASD-88-82 ARO-22684. 2-EG	F/G 11/6.1 NL

AD-A194 836	DYNAMIC FRACTURE TOUGHNESS EVALUATION BY MEASUREMENT OF CTD0 (CRACK TIP 0.) (U) JOHNS HOPKINS UNIV BALTIMORE MD DEPT OF MECHANICAL ENGINEERIN.. W N SHARPE ET AL.	1/1
UNCLASSIFIED	15 MAR 88 MMS/ASD-88-82 ARO-22684. 2-EG	F/G 11/6.1 NL

AD-A194 836	DYNAMIC FRACTURE TOUGHNESS EVALUATION BY MEASUREMENT OF CTD0 (CRACK TIP 0.) (U) JOHNS HOPKINS UNIV BALTIMORE MD DEPT OF MECHANICAL ENGINEERIN.. W N SHARPE ET AL.	1/1
UNCLASSIFIED	15 MAR 88 MMS/ASD-88-82 ARO-22684. 2-EG	F/G 11/6.1 NL

AD-A194 836	DYNAMIC FRACTURE TOUGHNESS EVALUATION BY MEASUREMENT OF CTD0 (CRACK TIP 0.) (U) JOHNS HOPKINS UNIV BALTIMORE MD DEPT OF MECHANICAL ENGINEERIN.. W N SHARPE ET AL.	1/1
UNCLASSIFIED	15 MAR 88 MMS/ASD-88-82 ARO-22684. 2-EG	F/G 11/6.1 NL

A 10x10 grid of 100 small images. Most cells are black. Some cells contain small white objects or patterns, including a small white object in the top-left, a small white object in the top-right, a small white object in the middle-left, a small white object in the middle-right, a small white object in the bottom-left, and a small white object in the bottom-right.



MICROCOPY RESOLUTION TEST CHART  
NATIONAL BUREAU OF STANDARDS 1963-A

AD-A194 836

②

Dynamic Fracture Toughness  
Evaluation by Measurement of CTOD

William N. Sharpe, Jr.  
Andrew S. Douglas  
Jason M. Shapiro

DISTRIBUTION STATEMENT A

Approved for public release;  
Distribution Unlimited

DTIC  
ELECTE  
MAY 11 1988  
S A H D



G.W.C. Whiting  
School of Engineering

The Johns Hopkins University

88 5 10 162

2

WNS/ASD-88-02  
February 1988

**Dynamic Fracture Toughness  
Evaluation by Measurement of CTOD**

William N. Sharpe, Jr.  
Andrew S. Douglas  
Jason M. Shapiro

**DTIC**  
**ELECTE**  
**S** **D**  
MAY 1 1 1988  
**H**

Department of Mechanical Engineering  
Room 127 Latrobe Hall  
The Johns Hopkins University  
Baltimore MD 21218  
(301) 338-7132

**DISTRIBUTION STATEMENT A**

Approved for public release;  
Distribution Unlimited

## I Abstract

Quantification of the dynamic fracture toughness of structural materials is essential to a wide range of problems—from nuclear accidents to ordnance applications. However, the difficulties associated with accurate measurements of cracks under dynamic loading are considerable. Thus there are no standardized procedures and few reliable results.

This work describes a systematic study of the dynamic fracture toughness of SAE-01 tool steel, 4340 and HY100 steels and a tungsten, using the ISDG (Interferometric Strain/Displacement Gage) system which has very high frequency resolution. The ISDG system is used to measure the crack tip opening displacement (CTOD) 100 microns behind a fatigue crack tip in a three-point bend specimen subject to a dynamic loading rate on the order of  $1 \times 10^6$  MPa $\sqrt{m/s}$ . Static measurements on similar specimens serve to calibrate the method and ensure consistency with the accepted procedures for static fracture toughness testing (ASTM E-399). Finite element analyses are used to obtain full field information at the point of initiation and to assess the material characteristics which lead to changes in toughness with loading rate.

The major advantage of the method is that information is obtained very close to the crack tip, so that stress wave loading effects are accounted for. A detailed error analysis gives an uncertainty of -10% to +20% in the determination of fracture toughness, which compares with  $\pm 20\%$  for published work.

Results show that 4340 steel, which is strain-rate insensitive, has no significant change in toughness with loading rate. Measurable toughness dependence on loading rate is found for HY-100 and tungsten, which are approximately 15% tougher under dynamic conditions. SAE-01 tool steel shows a significant increase (50%) in fracture toughness for dynamic over static loading.



Accession For	
NTIS GRA&I	<input checked="checked" type="checkbox"/>
DTIC TAB	<input type="checkbox"/>
Unannounced	<input type="checkbox"/>
Justification	
By _____	
Distribution/	
Availability Codes	
Dist	Avail and/or Special
A-1	

## **II Acknowledgements**

This research was supported by the Army Research Office under grant number DAAG-29-85-K-0218, in conjunction with the David Taylor Research and Development Center and the Aberdeen Proving Grounds.

Additional support for the computational investigation of viscoplastic effects was provided by the Office of Naval Research through contract number N00014-85-K-0711.

## Contents

<b>I Abstract</b>	<b>ii</b>
<b>II Acknowledgements</b>	<b>iii</b>
<b>1 Introduction</b>	<b>1</b>
<b>2 Background</b>	<b>3</b>
2.1 Dynamic Fracture Toughness Experiments . . . . .	3
2.2 Dynamic Fracture Analysis . . . . .	5
2.2.1 Theoretical Results . . . . .	5
2.2.2 Numerical Analysis of Fracture . . . . .	6
<b>3 Basics of the ISDG</b>	<b>8</b>
<b>4 Materials and Specimens</b>	<b>12</b>
4.1 Materials . . . . .	12
4.2 Specimens . . . . .	13
<b>5 Static Measurements</b>	<b>14</b>
5.1 Experimental Procedures . . . . .	14
5.2 Clip-Gage Results . . . . .	16
5.3 Load versus CTOD Results . . . . .	19
5.4 Compliances . . . . .	22
<b>6 Intermediate-rate Measurements</b>	<b>23</b>
6.1 Experimental Procedure . . . . .	23
6.2 Clip-gage Results . . . . .	24
6.3 CTOD Results . . . . .	25
6.4 Conclusions . . . . .	27
<b>7 High-Rate Measurements</b>	<b>28</b>
7.1 Developmental Tests . . . . .	28
7.2 Experimental Procedure . . . . .	31
7.3 CTOD versus Time Results . . . . .	36
7.4 Linearity of the Load Pulse . . . . .	36
7.4.1 Tup Strain Measurements . . . . .	38

7.4.2	Finite Element Analysis . . . . .	39
7.5	Load versus CTOD Results . . . . .	39
<b>8</b>	<b>Finite Element Computations</b>	<b>43</b>
8.1	Introduction . . . . .	43
8.2	Static Calculations . . . . .	43
8.3	Dynamic Calculations . . . . .	44
<b>9</b>	<b>Discussion of Results</b>	<b>46</b>
9.1	Static and Dynamic Load versus CTOD plots . . . . .	46
9.2	Critical Loads for the High-Rate Tests . . . . .	48
9.3	Fracture Surfaces . . . . .	52
9.4	Uncertainties of Measurement . . . . .	54
<b>10</b>	<b>Conclusions</b>	<b>56</b>
<b>11</b>	<b>References</b>	<b>59</b>
<b>A</b>	<b>Finite Element Computational Details</b>	<b>65</b>
A.1	General Modeling Procedures . . . . .	65
A.1.1	Mesh Details . . . . .	65
A.1.2	Time Integration . . . . .	68
A.1.3	Materials Response . . . . .	68
A.1.4	Impact . . . . .	70
A.2	Results of Static Calculations . . . . .	70
A.2.1	Tool Steel . . . . .	70
A.2.2	4340 Steel . . . . .	72
A.3	Results of Dynamic Calculations . . . . .	76
A.3.1	Tool Steel . . . . .	76
A.3.2	4340 Steel . . . . .	79
A.4	Post-processing . . . . .	79



# 1 Introduction

It is well-recognized that materials can behave differently under rapid loading; the effects are more pronounced in some materials than others. The study of dynamic stress-strain curves of metals was very active during the 1960s and has experienced somewhat of a revival in activity in recent years with the advent of new composite materials. Loading rate and temperature are closely coupled parameters in determining the deformation response of a material, and it is reasonable to expect that they are also important in the determining the growth of cracks or flaws in a structure or component. Indeed, this phenomenon has been established for structural steels for almost 20 years [2]. But, the test methods for measuring dynamic response of cracks in materials have not yet become established as they have for dynamic stress-strain response.

The implications of a difference in the response of a crack under dynamic loading are clear for both military and civilian applications. The military environment is likely to be more severe with the possibility of extremely high loading rates generated by explosives in contact. Slower rates would be produced by penetrators or projectiles. In the civilian sector, load transients (either planned or unexpected) can arise from a variety of sources such as power changes or accidents.

Just as the analytical solutions of fracture mechanics focus on the behavior at the critical point, i.e. the tip of the crack, experimental techniques should also examine this critical region. However, because of the scale of the dimensions involved, measurements "at the crack tip" have been made under dynamic loading in only a few cases. Near-tip experimental studies have been performed using a variety of techniques for static loading, but the complications associated with measurements on a time scale of microseconds have prohibited extensive study of corresponding dynamic loading. The requirements for measurements on a length scale of tens of micrometers over a time scale of tens of microseconds are challenging to the experimentalist.

The work reported here centers around the use of a unique laser-based interferometric technique to measure crack-opening displacement over just such scales. The measurements are closer to the crack tip than in other dynamic studies and for that reason alone are important as basic information about the physical behavior of a dynamically loaded crack. The crack-tip-opening displacement (CTOD) versus time plots can serve as "benchmark" data for finite element codes or theories that model the behavior of a rapidly loaded structure. But in addition, this data is converted into load versus CTOD plots for more direct comparison with static loadings and, to enable a measure of the dynamic fracture toughness.

Much of the effort associated with this project to-date has gone into the development of dynamic loading and recording techniques and procedures. SAE-O1 tool steel was used for specimens in this phase. The tests developed are an impact loading with a time scale of  $\sim 10$  microseconds and an intermediate-rate loading with a time scale on

the order of 50 milliseconds. The materials of interest are 4340 and HY-100 steel and tungsten.

An extensive background relating to the measurement and computation of dynamic crack behavior is presented in the next section. Section 3 follows with a description of the laser-based technique, referred to as the Interferometric Strain/Displacement Gage (ISDG). After a description of the materials and specimens in Section 4, the static tests, which are quite routine with the exception of the ISDG measurements, are presented. Section 6 describes the intermediate-rate tests which are not—as yet — entirely satisfactory. Section 7 describes the development of the dynamic tests and presents the time versus CTOD data. Procedures for converting this to a dynamic load-CTOD plot are described and that data presented. Dynamic finite element computation is a major effort in its own right, and the techniques and procedures used are described in Section 8. Finally, Sections 9 and 10 examine the data as a whole from the preceding sections and draw conclusions as to the dynamic fracture response of the four materials.

## 2 Background

Materials testing under conditions of high loading rates presents a real challenge to the experimentalist. One can extend the quasistatic loading techniques only so far before the effects of inertia and wave propagation come into play. Whereas procedures for measuring dynamic stress-strain curves have become more-or-less standardized over the years with the acceptance of the Hopkinson pressure bar, suitable techniques for the measurement of dynamic fracture toughness are still under study. This section of the report is a review of the experimental techniques that have been tried or are in use.

### 2.1 Dynamic Fracture Toughness Experiments

The effects of temperature and rate on the fracture toughness of structural steels were reported by Shoemaker and Rolfe [1]; these and similar results are also presented in the text by Rolfe and Barsom [2]. Dynamic  $K_{IC}$  values were obtained from three-point bend specimens that were impacted by a falling weight. These specimens were instrumented with foil strain gages placed adjacent to the crack tip and near the point of impact. Strains recorded dynamically were converted to load by assuming that the strain distribution was the same as that in an equivalent quasistatic test. The gage nearest the crack tip was used to determine when the crack started to propagate under the dynamic loading. The loading rates corresponded to a rate-of-change of the stress intensity factor of  $2 \times 10^5 \text{ MPa}\sqrt{\text{m/s}}$ .

Following the dynamic tests of Shoemaker and Rolfe, extensions of the familiar ASTM E-399 static fracture toughness tests were examined. This culminated in a round-robin evaluation [3] of tests conducted in high-speed closed-loop testing machines using clip gages to record the crack opening displacement. Compact and bend specimens of A533 steels were tested at rates on the order of  $1 \times 10^4 \text{ MPa}\sqrt{\text{m/s}}$ . The dynamic response of the clip gage is obviously of concern in these tests. The "ringing" observed in many results led to a proposal that an envelope be constructed around the rising portion of the displacement data; if the signal exceeds that envelope, the test would be invalid. Advantages of the approach are that it is an extension of a well-established standard, but the rate of test is much slower than achievable in other tests.

An impact test in which the loading tup is instrumented has the potential for measuring the load at which a crack in a pre-cracked specimen starts to propagate. Server [4] describes experiments on 3-point bend specimens loaded in a drop-weight tower at rates as high as  $1 \times 10^6 \text{ MPa}\sqrt{\text{m/s}}$ . Again, ringing of the load signal makes identification of the maximum load difficult.

A very clever dynamic fracture toughness testing method was developed by Costin *et al.* [5]. The specimen is a long rod with an annular precrack; this precrack is grown in fatigue in a specially developed rotating bending machine. The specimen is loaded by an explosive charge reacting against a mass fastened to one end of the rod. The rod

is instrumented with strain gages before and after the crack and with a unique optical gage for obtaining the opening displacement of the crack. A load-displacement curve can then be constructed and analyzed in the usual manner. Rates greater than  $1 \times 10^6$  MPa $\sqrt{\text{m}}$ /s were obtained; this corresponds to a loading pulse risetime on the order of 25 microseconds. This has become an established technique at Brown University where it has been used for a series of studies over the past 10 years. A similar setup is in use in France [6]. The major disadvantage with this testing method is the size of the specimen—a circular bar 25 mm in diameter by 1 meter long.

Klepaczko [7] has developed a version of the split Hopkinson pressure bar to measure the dynamic load-displacement curve of a wedge-loaded compact specimen. The system consists of an incident rod, the specimen, and a transmitter rod; both rods are instrumented with strain gages. The incident rod is impacted with a striker bar launched from a gas gun. Axial load and displacement can be obtained from the strain gage signals and used to compute the load-displacement curve. Rates on the order of  $1 \times 10^6$  MPa $\sqrt{\text{m}}$ /s were obtained and this approach has the advantage of a much simpler specimen.

A recent and intriguing technique is the 1-point bend impact test developed by Giovanola [8]. A simple edge-cracked specimen is placed in a Charpy machine, but there are no end supports. A strain gage mounted on the specimen records the deformation near the crack tip which is proportional to the stress intensity factor. Rates up to  $3 \times 10^6$  MPa $\sqrt{\text{m}}$ /s have been achieved.

The method of caustics can be used to determine stress intensity factors for both transparent and opaque materials. Most of the studies to-date concentrate on dynamically propagating cracks; the photography system is triggered by the initial crack movement. Ravichandar and Knauss [9] have measured the stress intensity factor history in plastic specimens at a rate on the order of  $1 \times 10^6$  MPa $\sqrt{\text{m}}$ /s. Their double-cantilever specimens were loaded by an exploding foil. Rosakis *et al.* [10] have used reflected caustics for dynamic stress intensity factor measurements in metals. The method of caustics, including dynamic testing, is described by Kalthof [11].

A modification of the Hopkinson pressure bar test has been developed by Kishida *et al.* [12] which uses a "hat-shaped" specimen. The striker bar hits the inside of the hat, generating a tensile pulse in the sides of the hat which have been precracked. Clearly the manufacture and precracking of such a specimen is complicated. Another version by the same group [13] uses one striker bar and two transmitter bars to record the load-displacement of a 3-point bend specimen. The measured loads are used in a dynamic finite element program to derive the critical fracture toughness.

There are several other novel optical methods for measuring the dynamic stress intensity factor in a specimen. Epstein [14] uses high resolution moire interferometry to measure the displacement field near the crack tip; a pulsed laser is used to take one photograph per test. Crostack [15] uses a similar pulsed laser system to take speckle photographs from which the displacements are calculated. Demler [16] photographs

microgrids with an image converter camera. Novinbakht [17] uses digital correlation of white light speckle patterns to measure the displacement field near the crack tip and uses a strobe light to illuminate the specimen. All of these techniques suffer from an inability to record data very rapidly; some only get data at one instant of time for each specimen.

## 2.2 Dynamic Fracture Analysis

Dynamic fracture covers both the propagation of cracks at velocities where material inertia and strain-rate sensitivity are important and the behavior of a stationary crack under impact or dynamic loading. Theoretical analyses of the dynamic fracture event have proven to be difficult. This is because the transient nature of the loading, the effects of material inertia, the complex material response to varying strain rates and highly nonproportional loading and the unsteady motion of the crack must be accounted for. Just as an understanding of the local fields surrounding a crack has proven so effective in static fracture, so too are asymptotic analyses of the dynamic fracture event essential to the understanding of dynamic fracture. Some of these results are reviewed below.

The impact of modern numerical methods (the finite element method in particular) on the analysis and understanding of fracture mechanics has been both profound and very wide in scope. This impact has been especially elucidating in nonlinear and dynamic problems where the classical analytical techniques have not been sufficient to reveal the fracture behavior and characterization.

### 2.2.1 Theoretical Results

For brittle materials, the concept of an elastic stress intensity factor,  $K$ , (which completely describes the local stress and deformation fields) has played a fundamental role—in both static and dynamic fracture [18,19,20]. In this case, crack propagation is governed only by the instantaneous value of the stress intensity factor and the material's resistance to either static or dynamic fracture. This is termed linear elastic fracture mechanics (LEFM). In order to predict crack growth, it is sufficient to know the instantaneous value of the stress intensity factor (a function of loading and geometry) and the resistance to fracture of that material.

In the dynamic fracture of laboratory scale specimens, conditions at the crack tip are determined by the boundary conditions through complicated stress wave interactions, making the calculation of the instantaneous stress intensity factor difficult. However, a number of significant contributions have been made, for example by Achenbach [21] and Knauss and Ravi-Chandar [22]. For some comments on the use of LEFM and its limitations, see Kanninen [23].

Clearly, LEFM is an idealization and it is necessary to consider the influence of plasticity on the local fields for static, quasi-statically growing and dynamically propagating

cracks. The stress and deformation fields in the region of plastic deformation are known only for power-law hardening materials under quasi-static proportional loading of a stationary crack. These local fields, the co-called HRR fields of Hutchinson [24] and Rice and Rosengren [25] are characterized by the parameter  $J$  which (for plane strain) can be determined by computing a path independent integral around the crack tip. Physically the  $J$ -integral is the energy release for a virtual crack extension [26].

In dynamic crack propagation, initial work by Rice [27] and Chitaley and McClintock [28] considered the asymptotic fields surrounding a quasi-statically growing crack in an elastic-plastic material. Slepyan [29] included the effects of material inertia, as did Dunayefsky and Achenbach [30] and Gao and Nemat-Nasser [31]. Hui and Riedel [32] considered creep crack growth, which was extended by Lo [33] to include inertia effects in cracks propagating at a steady velocity in viscoplastic materials.

The above results are restricted to the asymptotic fields surrounding a steadily propagating crack. The only indication of the extent of the asymptotic field is given by Freund and Douglas [34] for the special case of Mode III (antiplane shear) loading of a dynamic crack in an elastic-perfectly plastic material. Using the fracture criterion of McClintock and Irwin [35], Freund and Douglas were able to construct curves showing a theoretical rise in fracture toughness with increasing crack propagation velocity.

## 2.2.2 Numerical Analysis of Fracture

A number of numerical studies have been carried out to support and extend the analysis of dynamic fracture referred to above. For example, Freund and Douglas [36] extended their Mode III work to include the effects of strain-rate sensitivity. The Mode I calculations by Lam and Freund [37] for elastic-perfectly plastic (rate insensitive materials) also show an increase and compare favorably with experimental results. Details of the local fields near a rapidly propagating crack in a ductile material are discussed further by Freund *et al.* [38].

Of greater relevance to the work presented here, are the numerical simulations of fracture in both laboratory specimens and structural components subjected to dynamic loading conditions. Most simulations of structural dimensions are elasto-dynamic, for example Brickstad and Nilsson [39] consider crack propagation and arrest in pipes subjected to thermal and pressure loading (the "pressurized thermal shock" problem).

An experimental investigation, supported by finite element computations, of crack initiation under short pulse loading was done by Homma *et al.* [40]. The stress intensity factor (as a function of time),  $K(t)$ , was computed assuming elastic material response for pulse durations between 20 and 80  $\mu\text{s}$ . A review of short pulse fracture mechanics for elastic materials is given by Shockey *et al.* [41]. This was followed by a study by Homma *et al.* [42] on the minimum time for crack growth criterion in ductile materials. Here Homma *et al.* use power-law deformation theory to model the plasticity, but ac-

knowledge that they were only able "qualitatively to consider" the relationship between the minimum impulse duration and the time lag of the elastic-plastic stress history at the crack tip.

A numerical analysis of the dynamic fracture experiments on circumferentially notched round bars that are performed by Duffy *et al.* [43,44] has been done by Nakamura *et al.* [45]. This simulation use rate independent  $J_2$  flow theory plasticity to calculate the domain integral  $J$  [46] which characterizes the local fields surrounding the crack. The calculated  $J$ -integrals are compared with the deep crack approximations provided by Rice *et al.* [47]. The authors conclude that determination of the local  $J$ -integral is best done by measuring the notch opening, which gives more accurate results than those obtained by measuring the load point displacement. The fracture event takes place within  $50 \mu\text{s}$  and computations are based on a constant loading rate of  $4 \times 10^{12} \text{ N/s}$ .

Nakamura *et al.* [48,49] also analyzed the three-point-bend fracture specimen (which is similar to, but larger than the specimens used in this work) under dynamic loading. Their focus (just as in the case of the circumferentially notched round bar analysis) is on the relationship between physically measurable parameters and local crack fields. Since they are concerned with strain-gage measurements *remote* from the crack tip they conclude that these measurements are only applicable *after* wave reflections have died down and most of the dynamic transients are no longer present. Thus these measurements give valid fracture toughness measurements only if crack advance occurs after this "transition time".

### 3 Basics of the ISDG

The Interferometric Strain/Displacement Gage (ISDG) is a laser-based technique for measuring the relative displacement between two reflecting indentations on a specimen. These indentations are impressed into the specimen surface with a Vickers microhardness tester and are very small and close together. When they are illuminated with a laser, interference patterns form in space; motion of these fringe patterns is related to the change in distance between the indentations. Figure 1 is a schematic of the principle of the ISDG, and Figure 2 is a photomicrograph of a pair of indentations across a fatigue crack in the specimen.

When an indentation is illuminated with a laser beam perpendicular to the specimen surface, light is diffracted from each of the four triangular-shaped sides. Since the indents are so close together, the diffracted light rays overlap and interfere to form fringe patterns in space. The position of fringes of a given order in the patterns above and below the set of indents (as viewed in Figure 2) is proportional to the distance between the indents. This is simply the two-slit interference phenomenon of Young [64] except that it is in reflection, not transmission. The other two fringe patterns on either side of the indentations are not used in these measurements. The governing equation is:

$$d \sin \alpha = m \lambda \quad (3.1)$$

where  $\lambda$  is the wavelength of the laser,  $\alpha$  is the angle between the incident laser beam and the observation position, and  $m$  is the fringe order.

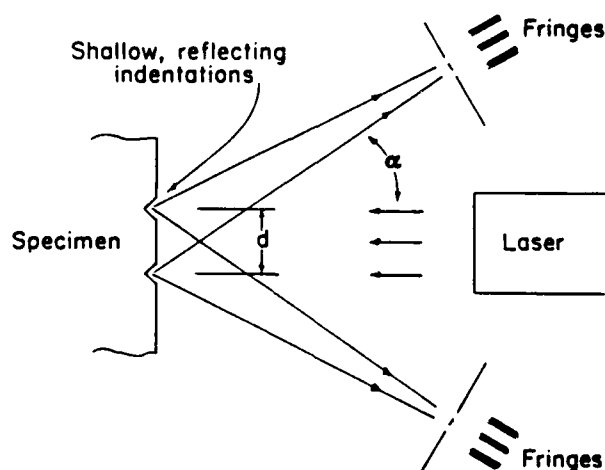


Figure 1: A schematic of the principle of the ISDG



It is the relative change in the distance between the indents that is of interest, and that change causes motion of the fringes. The interference fringes move within the diffraction pattern emanating from the individual indents. More details of the optical principles are given in [65]. The relation between the fringe motion and the relative displacement is given by:

$$\delta d = \frac{\delta M_1 + \delta M_2}{2} \frac{\lambda}{\sin \alpha_0} \quad (3.2)$$

where  $\alpha_0$  is the angle between the incident laser beam and the fringe patterns, and  $\delta M_1$ ,  $\delta M_2$  are the relative fringe motions. "Relative fringe motion" means the displacement of a fringe divided by the distance between it and the next fringe.

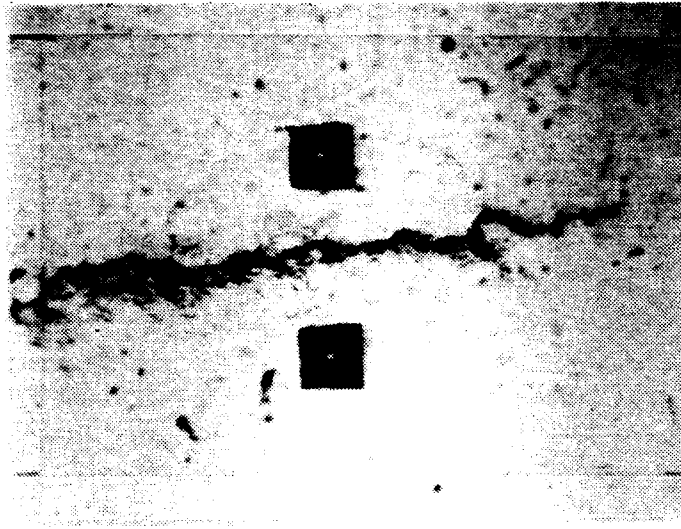


Figure 2: A pair of indentations across a fatigue crack. The indents are  $70 \mu\text{m}$  apart and are each approximately  $20 \mu\text{m}$  square and  $4 \mu\text{m}$  deep.

It is necessary to monitor both fringe patterns to avoid errors from rigid-body motion of the specimen. As Equation 3.1 shows, a separation of the indents causes both sets of fringes to move toward the incident laser beam. A rigid-body motion in the vertical direction in Figure 1 would cause one set of fringes to move toward the beam and the other to move away from it. By averaging the total fringe motion of the two patterns, one eliminates the effects of rigid-body motion in a direction parallel to the line between the two indents; however, other components of rigid-body motion will cause errors.

The wavelength of a He-Ne laser is  $0.6328 \mu\text{m}$ , and  $\alpha_0$  is typically  $42^\circ$ . The quantity  $\lambda/\sin \alpha_0$  is then  $0.94 \mu\text{m}$ ; this means that an average relative fringe motion of 1

corresponds to a relative displacement of  $0.94 \mu\text{m}$ . If one places a detector at a fixed position,  $\alpha_0$ , and observes the intensity to change from dark to bright and back to dark, then one has observed a relative displacement between the two indents of  $0.94 \mu\text{m}$ . The intensity changes recorded by the detector will have a generally sinusoidal shape although the period will not be constant unless the displacement is changing linearly with load or time. Since it is easy to identify maxima and minima of the recorded signal, the basic resolution of the measurement is approximately  $1/2 \mu\text{m}$ .

All that is needed to make an ISDG measurement is a pair of photodetectors with adequate frequency response and a suitable recording system. The recording system could be a stripchart recorder, a minicomputer-based data acquisition system, or an oscilloscope—depending upon the time scale of the measurement. The steps in obtaining a plot of load or time versus displacement are:

1. Record the fringe motion of both patterns as a function of load or time.
2. Read the locations of the maxima and minima as a function of load or time.
3. Multiply the fringe shifts (in increments of  $1/2$ ) by the calibration factor  $\lambda / \sin \alpha_0$  and plot these points versus load or time.
4. Average the displacement plots from the two fringe patterns at increments of load or time.

Note that it is the location of the maximum or minimum that is measured, not its magnitude; therefore, the illuminating laser beam does not have to be uniform in intensity.

The measurement system employed in this work is simply a modern version of one used earlier by Sharpe [66]. That system was used to measure dynamic plastic strain in aluminum specimens subjected to impact. A total fringe shift on the order of two or three fringes was observed, so the technique did not have very good resolution. In this work, the displacements are almost a factor of ten larger, so the resolution is adequate.

Primary advantages of the ISDG are: a short gage length, no contact with the specimen, and high frequency response. The gage length can be as short as  $25 \mu\text{m}$  in typical applications, but the spacing between indents is  $70 \mu\text{m}$  for these tests. The noncontacting feature means that the gage can be used in hostile environments such as high or low temperature or in the presence of rapidly varying electromagnetic fields. The frequency response depends upon the photodetectors and the recording system, so a very inexpensive setup can be used for quasistatic tests. At higher rates, readily available photomultiplier tubes and oscilloscopes are adequate.

The basic resolution is determined by the calibration factor  $\lambda / \sin \alpha_0$  and is approximately  $0.5 \mu\text{m}$  because one counts both maxima and minima on the fringe record. A

minicomputer-based system [67] that has a resolution of  $0.02 \mu\text{m}$  is used for fatigue studies. The uncertainty in the displacement values come from the measurement of  $\alpha_o$  and the identification of the location of the maxima and minima.  $\alpha_o$  can be measured to  $1/2$  degree with no difficulty which yields an uncertainty in the calibration factor of  $\pm 1$  percent. The maxima/minima can be located within  $\pm 0.02$  of the fringe spacing which corresponds to an uncertainty of approximately  $\pm 0.02 \mu\text{m}$ . So, the uncertainty in a displacement measurement is:

$$\Delta d = 0.01 \times \delta M_{ave} \frac{\lambda}{\sin \alpha_o} + 0.02 \quad (3.3)$$

For example, a measured displacement of  $1 \mu\text{m}$  would have a relative uncertainty of  $\pm 3$  percent; whereas, a measured displacement of  $10 \mu\text{m}$  would have a relative uncertainty of  $\pm 1.2$  percent.

## 4 Materials and Specimens

### 4.1 Materials

Four materials were used in this study: SAE-01 tool steel, 4340 steel, HY-100 steel, and tungsten. The tool steel was used for the development of the techniques used in the tests because it is readily available in bar stock of a suitable size. The dynamic experiments in particular required several tests to perfect the triggering and recording instrumentation and procedures. There is more data of a similar nature available for 4340 steel than any other material, so it was tested to provide comparison of the results with those of other workers. The tungsten is of interest to the Army because it is used in penetrators, and HY-100 is important to the Navy because of its use in ship hulls. The tungsten and HY-100 stock were provided by Aberdeen Proving Ground and DTNSRDC respectively, and the other two steels were purchased locally.

Stress-strain curves of the four materials are presented in Figure 3. The tool steel stress-strain curves was measured locally, but the other three were measured by Metcut Associates of Cincinnati, OH who machined specimens from those materials.

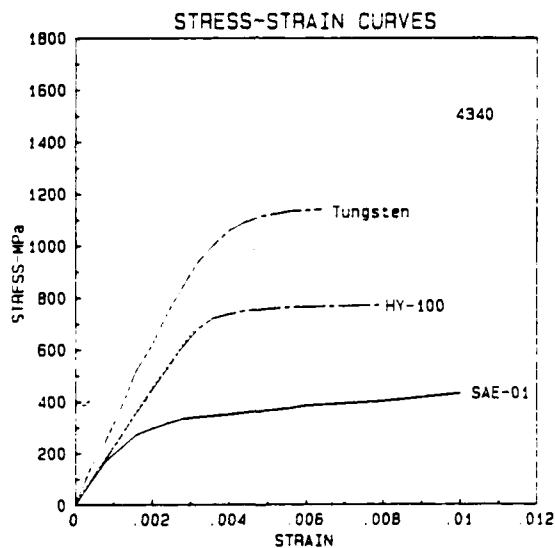


Figure 3: Stress-strain curves of the four materials.

The material properties are given in Table I.

Table I

Material	Elastic Modulus 1000 MPa	0.2% Yield Stress MPa	Hardness Rockwell C
SAE-01	213	345	14
4340	226	1530	52
HY-100	223	765	24
tungsten	316	1130	39

## 4.2 Specimens

A drawing of the 3-point bend specimens is given in Figure 4; it is the standard geometry as specified by ASTM E-399. The metric dimensions are a span of 50 mm, a thickness of 6.35 mm and a height of 12.5 mm. As noted above, Metcut Associates machined the 4340, HY-100 and tungsten specimens. The tool-steel specimens were machined locally.

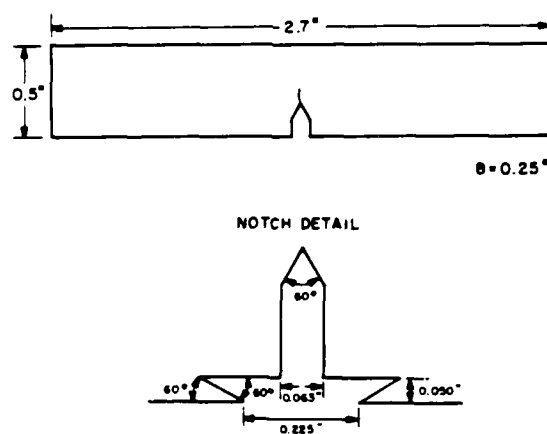


Figure 4: Dimensions of the 3-point bend specimen.

The precracking procedures closely followed those in E-399 in that the final values of the applied stress intensity were kept less than 60 percent of the anticipated fracture toughness. The precracking is important because, as will be seen, the closure load is a reasonable fraction of the applied load, and uniformity of the closure loads is preferred.

Following the specimen machining and precracking, they were polished using typical metallurgical procedures with various grits of sandpaper and a final polish of 0.5 micron diamond paste. Indents were then applied with a LECO microhardness tester at the standardized position at 100  $\mu\text{m}$  behind the crack tip with a spacing of 70  $\mu\text{m}$ .

## 5 Static Measurements

The static tests on the 3-point bend specimens were conducted in an electrohydraulic test machine with the fringe motions measured by photoresistors and recorded by a minicomputer. At the same time, the crack-mouth opening displacement was recorded with a clip-gage; this load-displacement plot was used to establish the critical load,  $P_q$ , by following the ASTM E-399 procedures.

### 5.1 Experimental Procedures

Figure 5 is a schematic of the experimental setup, and Figure 6 is a photograph of the overall arrangement. The test machine is an MTS 100-kip capacity frame with a 20 kip actuator and load cell, and is controlled by the 448 series of electronics. A 10 gpm hydraulic pump powers the system. As shown in Figure 6, the specimen sits on a roller support attached to the ram of the machine, and the tup is attached to the load cell. The rollers are 50.8 mm apart, and the dimensions of the roller support meet the requirements of ASTM E-399. The radius of the steel tup is 8 mm as required by E-399.

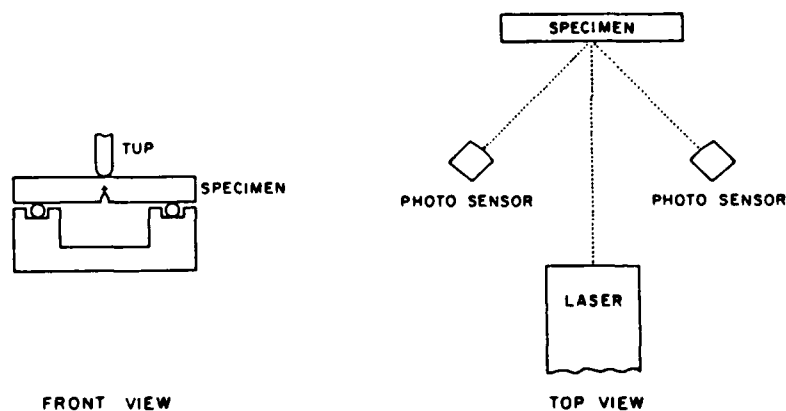


Figure 5: Schematic of the static setup.

Crack mouth opening displacement was measured with a foil-gage-based clip-gage manufactured in accordance with E-399. The foil gage bridge was powered by a Measurements Group model P-3500 strain indicator, and the analog voltage output was amplified with a Tektronix model AM-502 amplifier prior to input to the minicomputer.

Fringe intensity was measured with cadmium sulfide photoresistors (model 276-116A from Radio Shack) connected through a simple resistive circuit that produced a voltage

output on the order of 2 volts. These signals were also conditioned by AM-502 amplifiers. The indentations on the specimen were illuminated by a 15 milliwatt He-Ne laser (Spectra-Physics model 124B).

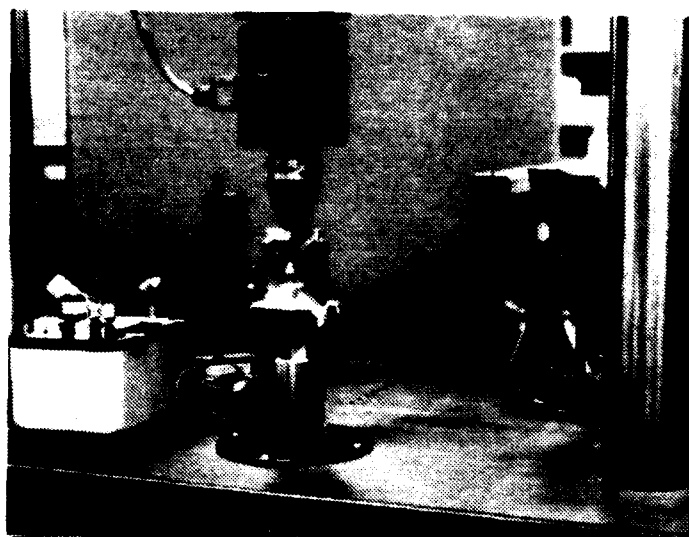


Figure 6: Photograph of the static setup.

The minicomputer used is an IBM/AT with an analog/digital interface board from Data Translation, Inc. (model DT2821). A load signal was sent to the MTS machine through D/A #0 to control the load on the specimen. The signal from the load cell, the intensity from the two photoresistors, and the voltage from the clip-gage were recorded via A/D #0,1,2,3 for each increment of applied load.

The entire test was controlled by the minicomputer using a program named RUNTEST which was written in Microsoft FORTRAN using routines from the ATLAB software provided with the Data Translation board. The simple strategy was to send out a load signal to the test machine and then record the four voltage signals; this step was repeated 500 times. These static tests took 190 seconds which produces a loading rate consistent with E-399; however, RUNTEST can conduct a test with a duration as short as 10 seconds. Data was stored on the fixed disk of the IBM/AT and backed up on diskettes.

Figure 7 is a plot of a typical fringe intensity record; the signals have been shifted on the voltage scale for clarity in presentation. Note that the magnitude of the signal is

not important (the voltage range in Figure 7 is 5 volts); only the position of the maxima and minima of the fringes is needed. This data is converted into a load-displacement plot via a computer program that locates and stores the max/min positions and then multiplies them by the appropriate calibration factor. The two load-CTOD records are then plotted and averaged manually (because the average should be done at increments of load—not displacement) to produce the final load-CTOD plot. The fringe record in Figure 7 is used to produce the load versus CTOD plot for test COD 18 in Figure 15.

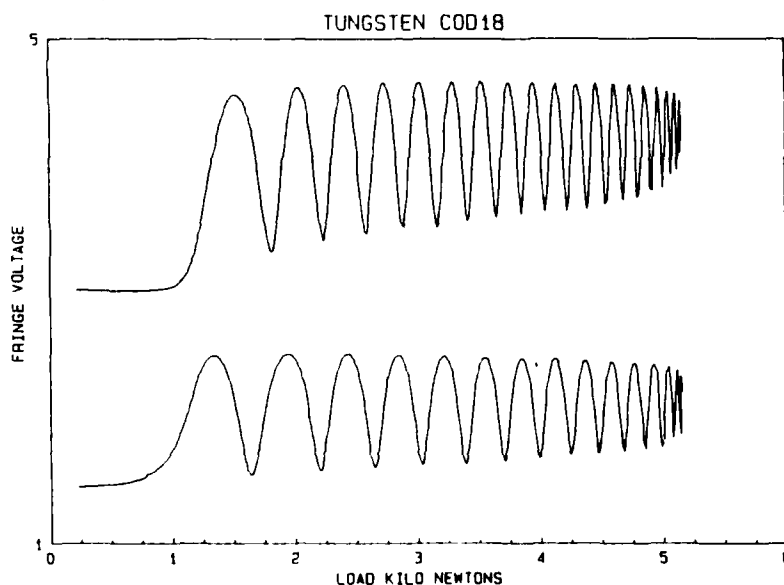


Figure 7: Typical records of fringe intensity versus load.

## 5.2 Clip-Gage Results

The clip-gage results are quite routine, but they are presented here because they provide the static values of  $P_q$  and are central to the comparisons with the dynamic measurements.

The clip-gage plots for the two SAE-01 specimens are shown in Figure 8. The original slope and the 5 percent reduced slope are also shown on the figure. Although the readings for COD05 were quite noisy, the curve was nearly identical to the one for COD06, and they both had the same value of  $P_q$ .

Clip-gage data for 4340 is shown in Figure 9. The 4340 was quite brittle, so the clip-gage reading stopped suddenly when the specimen broke. The values of  $P_q$  are shown on the plot.

A clip-gage plot for two HY-100 specimens is shown in Figure 10. It is clear in this case of HY-100 that the conditions of plane strain fracture toughness are not met. The same is true for the SAE-01 specimens, but the 4340 and the tungsten are brittle



enough that a legitimate  $P_f$  is obtained. Figure 11 is a plot of the clip-gage record for tungsten; note the two linear slopes are slightly different for the two specimens.

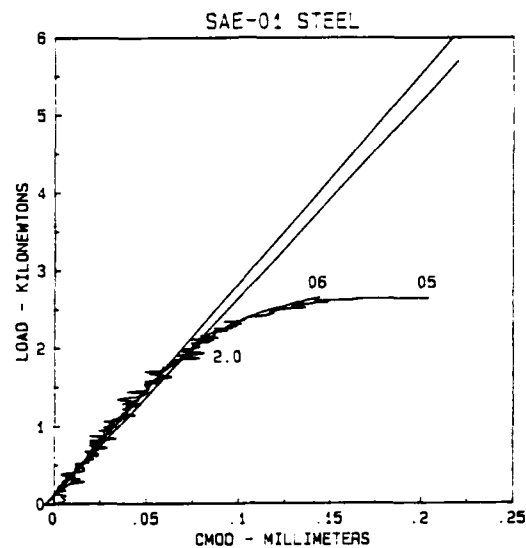


Figure 8: Clip-gage record for SAE-01

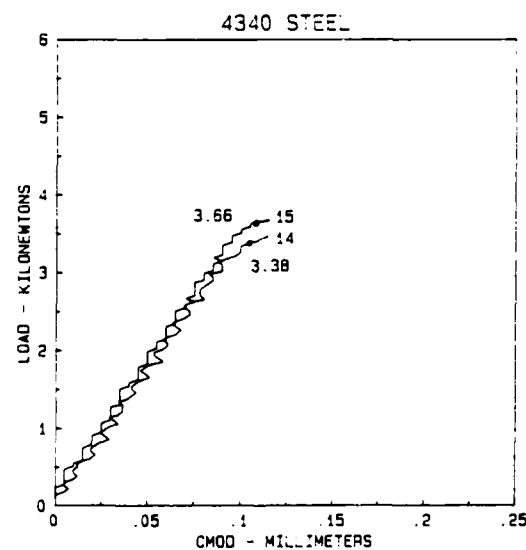


Figure 9: Clip-gage record for 4340 Steel

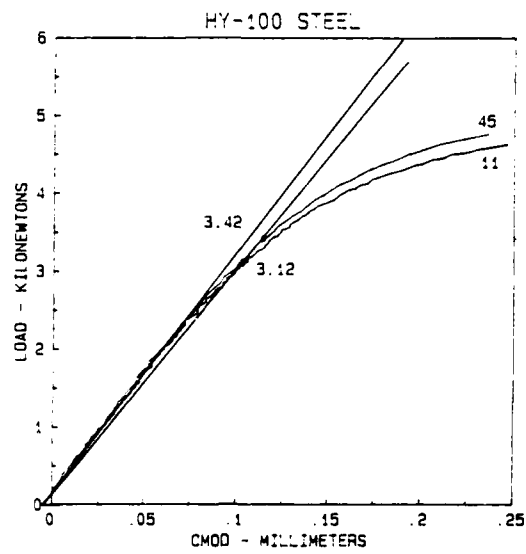


Figure 10: Clip-gage record for HY-100 Steel

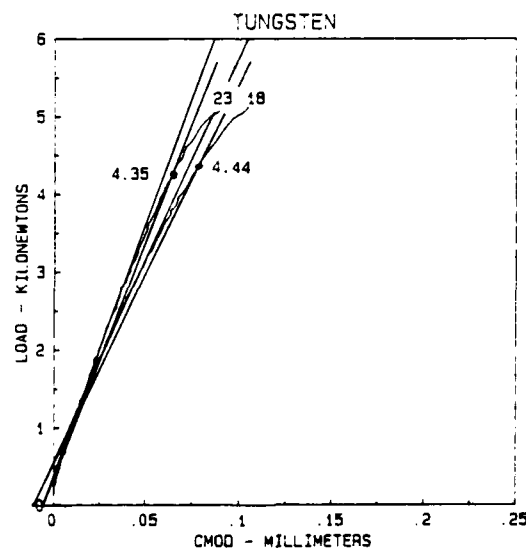


Figure 11: Clip-gage record for tungsten

### 5.3 Load versus CTOD Results

The static load-CTOD data for the four materials are shown in Figures 12 through 15. The relative uncertainty in the CTOD is  $\pm 3$  percent and arises from the uncertainty in determining the initial angles of the fringe patterns and the variability in identifying the locations of the maxima and minima. The closure load is evident in each of the plots; it varies somewhat because of variations in the pre-cracking procedure. Table II lists the physical and geometrical data for each of the specimens. The crack length listed in the table is the average at the center and two quarter-points taken in accordance with ASTM E-399 after the specimen was broken.

Table II

Specimen Number	Material	Crack Length mm	$P_q$ kN	$K_q$ MPa $\sqrt{m}$
COD 5	SAE-01	6.54	2.00	31.2
COD 6	SAE-01	7.00	2.00	35.2
COD 14	4340	6.41	3.38	51.0
COD 15	4340	6.45	3.66	58.9
COD 11	HY 100	6.64	3.12	49.9
COD 45	HY-100	6.88	3.42	58.5
COD 18	Tungsten	6.16	4.44	63.0
COD 23	Tungsten	6.19	4.35	62.5

The SAE-01 steel is a very ductile material, and shows a lot of plasticity as seen in Figure 12. The two load-CTOD plots are very nearly identical with the principal difference caused by the difference in closure loads arising from the precracking procedures. Fatigue cracks in specimens simply do not grow identically, and slight differences in load shedding affect the closure load.

The 4340 steel is more brittle and shows a longer linear region of elastic behavior. Note the pronounced nonlinear behavior at the crack tip above 1.5 kN in contrast to the almost completely linear behavior measured with the clip-gage.

HY-100 steel is also quite ductile and stronger than the SAE-01. The nonlinear behavior at the tip starts sooner than it does at the crack mouth. Tungsten is a stiff, strong, brittle material, and except for a difference in the closure loads, the results are quite reproducible.

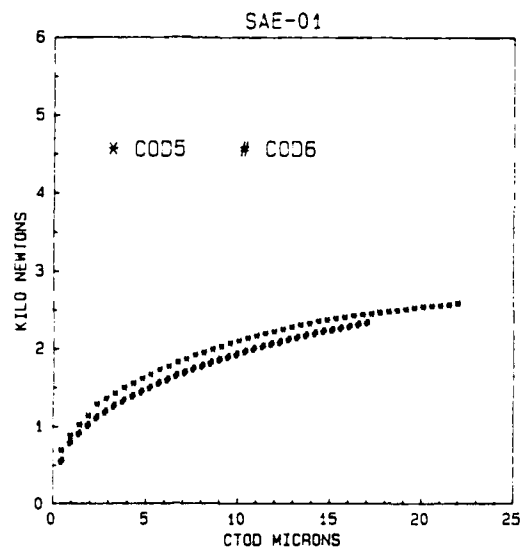


Figure 12: Load versus CTOD records for SAE-O1 steel.

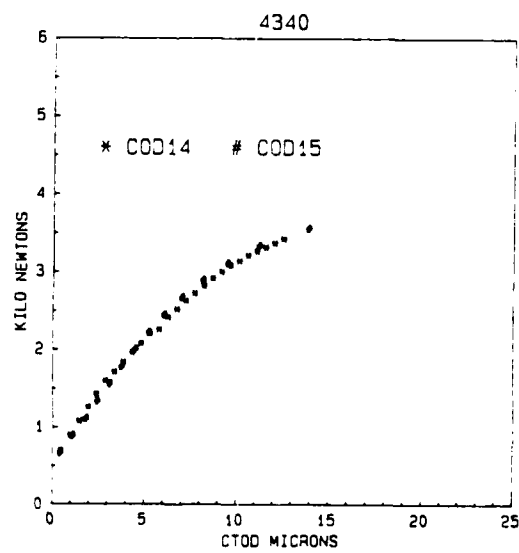


Figure 13: Load versus CTOD records for 4340 steel.

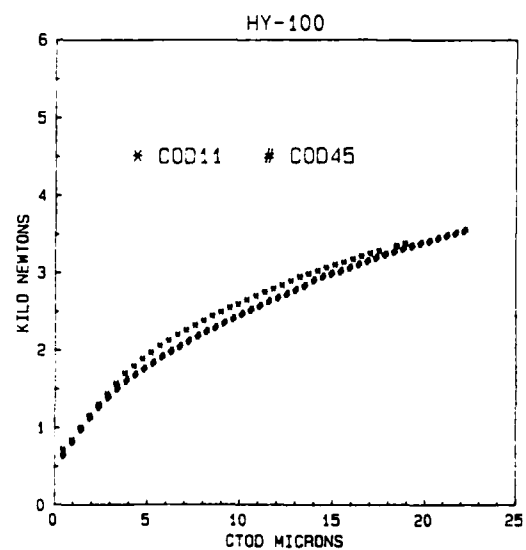


Figure 14: Load versus CTOD records for HY-100 steel.

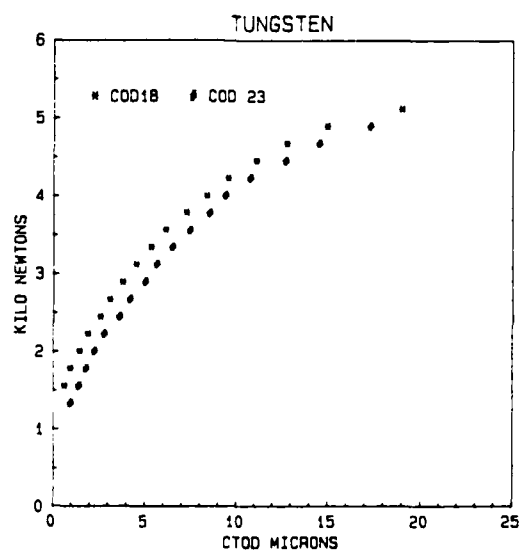


Figure 15: Load versus CTOD records for tungsten.

## 5.4 Compliances

Table III contains a listing of the measured and calculated compliances for these static tests. The "measured compliance" is obtained from the slope of the initial linear region of the plots in the preceding figures. The calculated compliances are from the formula:

$$u_y/P = \frac{S}{BW^{3/2}G} \sqrt{r/2\pi} F(\theta) G(a/W) \quad (5.1)$$

where  $u_y$  is the vertical displacement of the crack (half the displacement measured by the ISDG),  $P$  is the load,  $S, B, W$  are the span, thickness, and width of the specimen respectively, and  $F(\theta)$  and  $G(a/W)$  are given in ASTM E-399.  $F(\theta)$  is computed using the location of the indent at  $100 \mu\text{m}$  behind the crack tip and  $35 \mu\text{m}$  above the plane of the crack. Calculations are presented based on either plane stress or plane strain behavior.

Table III

Specimen Number	Measured Compliance $\mu\text{m}/\text{kN}$	Plane Strain Compliance $\mu\text{m}/\text{kN}$	Plane Stress Compliance $\mu\text{m}/\text{kN}$
COD 5	3.00	2.30	2.08
COD 6	3.28	2.56	2.32
COD 14	2.78	2.02	1.83
COD 15	2.78	2.15	1.95
COD 11	3.26	2.19	1.98
COD 45	3.26	2.17	1.97
COD 18	1.75	1.33	1.21
COD 23	1.75	1.34	1.21

The measured compliances are quite consistent and are always larger than the calculated compliances. This indicates that the effective length of the crack (as regards these compliance calculations) is somewhat longer than the surface crack. It is, of course, because the crack is bowed forward in the center of the specimen. In fact, if one assumes that the effective length of the crack is  $100 \mu\text{m}$  longer than the surface crack, one simply multiplies the calculated values by  $(200/100)^{1/2}$  and obtains reasonable agreement with the measured values. Given the fact that the indents are within  $\sim 100 \mu\text{m}$  of the crack tip in a specimen that is  $6,350 \mu\text{m}$  thick, the agreement among the measured and calculated compliances is actually quite good. It would be difficult to use the compliance measured so close to the crack tip to accurately predict the crack length, but they are a very sensitive indicator of *changes* in crack length.

## 6 Intermediate-rate Measurements

The experimental setup for the intermediate-rate tests was basically the same as for the static tests except that the photoresistors were replaced with photomultiplier tubes (PMTs) for better frequency response. In addition, a different data acquisition program was written. Tests were run on the four materials, and the plots of load versus CMOD from the clip-gage were similar to the static tests. This indicated that the frequency response of the test system was adequate. However, the CTOD data from the ISDG showed initial loads and slopes that were not consistent with the static results.

### 6.1 Experimental Procedure

The photomultiplier tubes are RCA 4840s with model PF 1042 power supplies which are powered by 13.5 volts DC. The apertures were covered with interference filters and were also masked except for slits approximately 1.5 mm wide. The low-level voltage signals from the tubes were inverted and amplified via the Tektronix AM-502 amplifiers. The upper frequency limit of the amplifiers was set at 10 kHz. The photomultiplier tubes were mounted on translation stages to permit manual scanning across a fringe pattern during setup of the test (just as for the photoresistors in the quasi-static tests).

A different computer program was written for these faster tests. The strategy was to initiate the test with the START button of the test machine and record the four voltage signals (from the load cell, the clip-gage, and the two PMTs) using the direct memory access (DMA) feature of the Data Translation board. Four channels can be sampled at a thru-put of 30 kHz which translates to a sampling rate of 7.5 kHz per channel. This program, called FASTRUN, is set to take 1200 data points, so the recording time is approximately 160 milliseconds. Data acquisition is initiated by continually sampling the load signal until it changes by 10 bits (56 N) after the START button is pushed—at which point the computer is instructed to save the next 1200 points.

For all these tests, the first ramp time on the MTS controller was set at 0.110 seconds, and the second ramp frequency was set at  $2.0 \times 10^4$  Hz (although this falling portion of the input pulse doesn't matter). The load range of the MTS was set for 11.125 kN (2500 pounds), so the input electrical pulse called for a linear rise at a rate of 101 kN/s; that is 11.125 kN (2500 pounds) divided by the specified duration of the ramp which was 0.11 seconds. Since the expected maximum loads were on the order of 3–5 kN, the risetime of the load pulse was expected to be  $\sim 40$  milliseconds. The upper limit was set 25 percent higher than the anticipated maximum load so that the ram wouldn't push further into the fixture after the specimen had broken.

Figure 16 is a record of load versus time for a test (INT35) on SAE-01 tool steel; it is typical of the records from the other intermediate-rate tests. The input signal from the function generator of the test machine is drawn on the plot. The inertia of the ram and the hydraulic system prevents the load signal from following the input signal at

this high rate. The load cell is model 3116-5K from Eaton, Inc. and has a specified frequency response of 600 Hz. Theoretically, this is high enough to follow a signal with a risetime on the order of one millisecond. The loading in Figure 16 turns out to be equivalent to a loading rate of approximately  $500 \text{ MPa}\sqrt{\text{m/s}}$ .

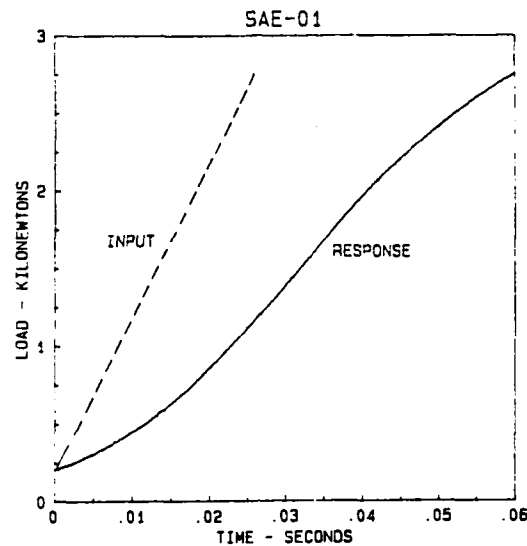


Figure 16: Load versus time as measured by the load cell and as input by the signal generator.

## 6.2 Clip-gage Results

The CMOD was measured with the same clip gage and instrumentation as used in the static tests. The frequency response of the P-3500 unit is 3dB at 4 kHz, so it too is fast enough for these tests.

Figure 17 is a plot of a clip gage result for the SAE-01 tool steel. It is very similar, in fact nearly identical, to the equivalent static plot. This indicates that not only the signal conditioner, but the clip gage itself, has adequate frequency response. However, there was some difficulty in these tests with the clip gage slipping in the grooves and giving erratic data.



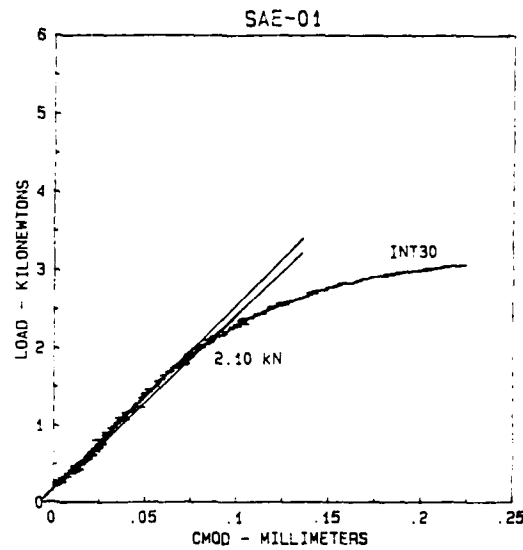


Figure 17: Clip gage results at the intermediate rate.

Table IV gives the  $P_q$  values from the intermediate-rate tests.

Table IV

Test Number	Material	Crack Length mm	$P_q$ kN	$K_q$ $\text{MPa}\sqrt{\text{m}}$
INT30	SAE-01	6.82	2.10	35.3
INT35	SAE-01	6.75	2.15	35.5
INT41	4340	6.59	3.30	52.2
INT42	4340	6.86	3.35	56.6
INT39	HY-100	6.71	4.00	65.3
INT40	HY-100	6.68	4.57	77.7
INT44	Tungsten	6.23	3.28	47.3
INT46	Tungsten	6.23	3.81	54.9

The results for SAE-01 and 4340 are similar to the static results; however, the HY-100 values are considerably higher and the tungsten values considerably lower than their static counterparts.

### 6.3 CTOD Results

Figure 18 is a plot of two fringe intensities versus the input load. In all of these intermediate-rate tests, a small preload of approximately 0.15kN (30 pounds) was ap-

plied to the specimen before the test was started. Then, the data acquisition did not start until another 0.06 kN was applied. This is why the fringe signals do not start at zero load in the figure.

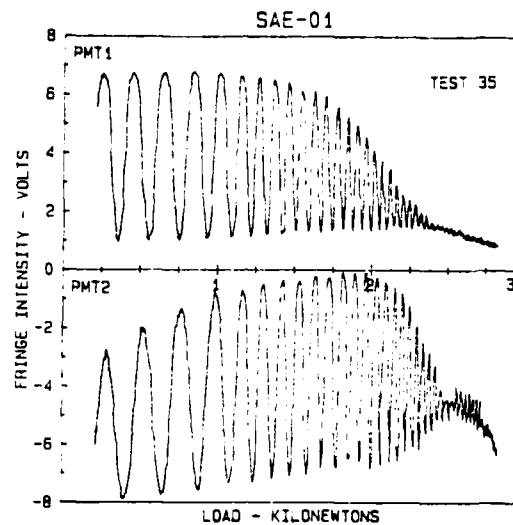


Figure 18: Fringe intensities at the intermediate rate.

The troubling part about Figure 18 is that the fringe intensities do not start at a minimum at the initial load. All intermediate-rate tests had the fringe signals set to zero initially, and all showed a similar behavior to that seen in Figure 18. The corresponding load-CTOD plot is shown in Figure 19 which also presents another test on the SAE-01 steel.

This phenomenon produces load-CTOD curves that start at a lower value and have a higher compliance than do the static counterparts. Table V summarizes the results of the intermediate-rate tests and compares them with the static ones. The "Load at first max" is the load at which the first maximum in fringe intensity is observed. The intermediate-rate and the static results might very well be different, but the differences seen here are not reasonable. There is no reason for the fringes to shift before the load is applied, and there is no reason for the initial linear response of the specimen to be different. One must conclude that the load cell is not accurately measuring the input at the crack tip in this testing arrangement at this rate. It appears that the crack tip is subjected to a load pulse which is not sensed immediately by the load cell; this is not unreasonable given the reasonably high rate of loading.

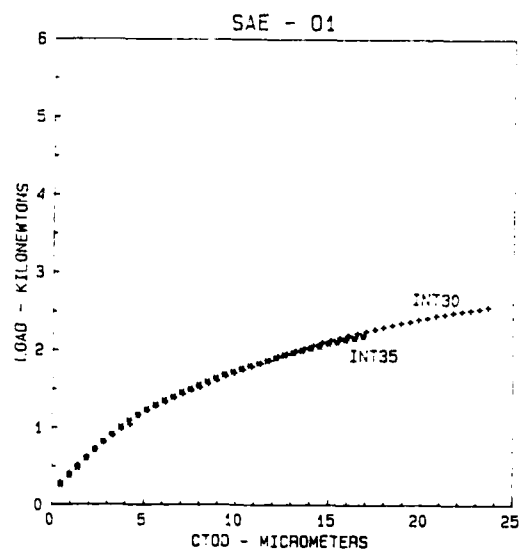


Figure 19: Load versus CTOD for two intermediate-rate tests on SAE-01 steel.

Table V

Test Number	Load at first max kN	Static Counterpart kN	Compliance $\mu\text{m}/\text{kN}$	Static Counterpart $\mu\text{m}/\text{kN}$
INT30	0.30	0.69	4.44	2.08
INT35	0.26	0.56	4.44	2.32
INT41	0.23	0.70	4.13	1.83
INT42	0.24	0.45	3.63	1.95
INT39	0.44	0.72	2.94	1.98
INT40	0.26	0.26	2.94	1.97
INT44	0.62	1.43	2.32	1.21
INT46	0.63	1.08	2.32	1.21

#### 6.4 Conclusions

Although the clip gage data seems reasonable, the CTOD data does not. These tests are run at a rate at which the dynamic effects of the testing machine must be considered. The data obtained here should not be regarded as valid, but should serve as a guide to further study of test procedures at these intermediate rates.

## 7 High-Rate Measurements

Measurement of the CTOD at the surface of a specimen near the tip of a crack is a unique experimental approach, and the techniques and procedures in the two previous sections have required considerable developmental efforts. When one extends these to high-rate loading (which is really the area of interest), the techniques and procedures become even more sophisticated. High-rate deformation was achieved by firing a projectile into a 3-point bend specimen and recording the fringe motions on an oscilloscope. This information is used to produce a record of CTOD versus time. The initial linear slope of the resulting CTOD versus time record is then taken as the linear loading rate applied to the specimen up to the point of crack initiation. This enables the construction of a load versus CTOD record which can then be compared with similar records obtained at slower rates.

### 7.1 Developmental Tests

Since these measurements and the associated techniques are new, quite a bit of initial effort went into developing the final test procedure. It is probably useful to include a discussion of these developmental efforts because they give background to the final test and analysis procedures which are described in the following section. The original tests were done at Aberdeen Proving Ground using explosives, and these proved the feasibility of the approach. The final experimental setup used a gas gun at the Johns Hopkins University. The safety procedures required for explosive testing make a gas gun an attractive alternate. Further, the advantage of having the testing facility located on campus is important when working with students.

The first dynamic tests were conducted in an explosive chamber at Aberdeen Proving Grounds with the cooperation of Mr. Paul Netherwood. A schematic of the setup is shown in Figure 20. An explosive detonator was fastened to a 6.3 mm tup which was then placed in contact with the specimen. The detonator was fired by a 22.5 volt signal. A twisted pair of varnish-coated trigger wires was wrapped around the detonator and connected in series with a battery to the external trigger of the oscilloscopes. When the detonator fired, it vaporized the varnish, shorting the circuit and triggering the oscilloscopes. Both a Tektronix 555 analog oscilloscope with camera and a Nicolet digital oscilloscope with a model 205-A plug-in were used; the experience with the Nicolet influenced the decision to purchase a LeCroy digital oscilloscope for the gas gun tests.

A major problem with the explosive tests was the flash associated with the detonator. By using mirrors to direct the fringe patterns so that the PMTs did not point directly at the flash and by masking the plexiglas port down to very small apertures, it was possible to get good fringe signals. Figure 21 is a photograph of a pair of fringe versus time traces taken from the Nicolet.

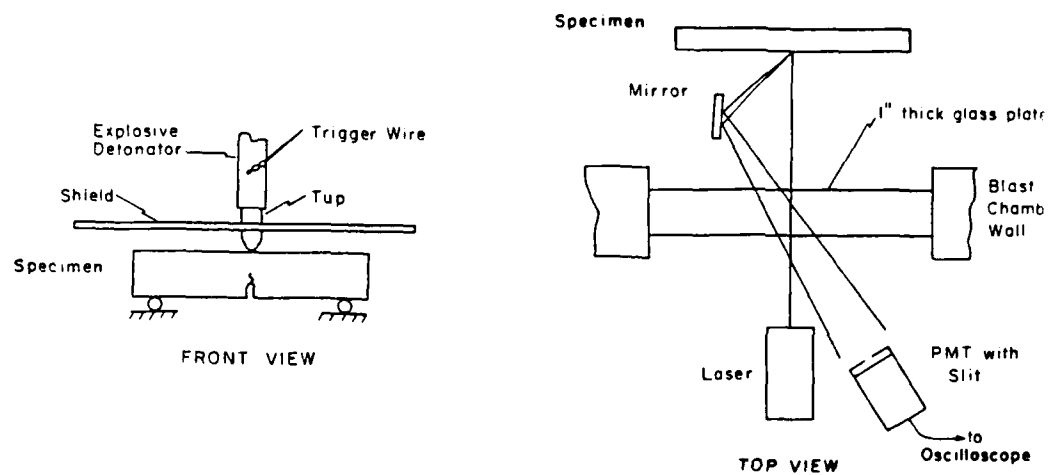


Figure 20: Schematic of the explosive test setup.

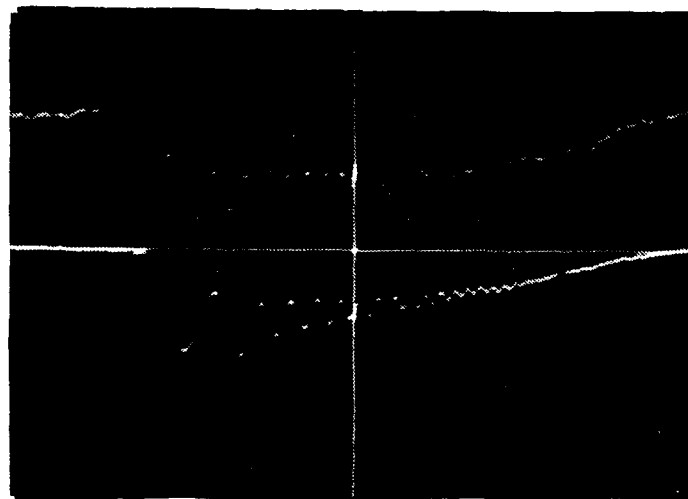


Figure 21: Fringe intensity versus time from an explosive test. The signals have been expanded after the test, and the total time span in the photograph is  $20 \mu s$ .

The original plan was to have two sets of indents across the fatigue precrack—one set  $100\text{ }\mu\text{m}$  and another set  $200\text{ }\mu\text{m}$  behind the crack tip. This would enable a measurement of the crack tip opening angle (CTOA). It is necessary to tilt each set of indents relative to a normal to the specimen so that the fringe patterns from them do not overlap. Figure 22 is a photomicrograph of two sets of tilted indents. Four PMTs are required for such a test, and Figure 23 is a plot of the two measured CTODs (these experiments were performed in the explosive test chamber). It was hoped that by measuring the angle, one could determine when the crack started to move, i.e. once the angle began to project to a point ahead of the original tip, it would be assumed that the crack had initiated. However, the uncertainty associated with the angle determination and the inability to differentiate plastic deformation at the tip from crack advance rendered this approach ineffective.

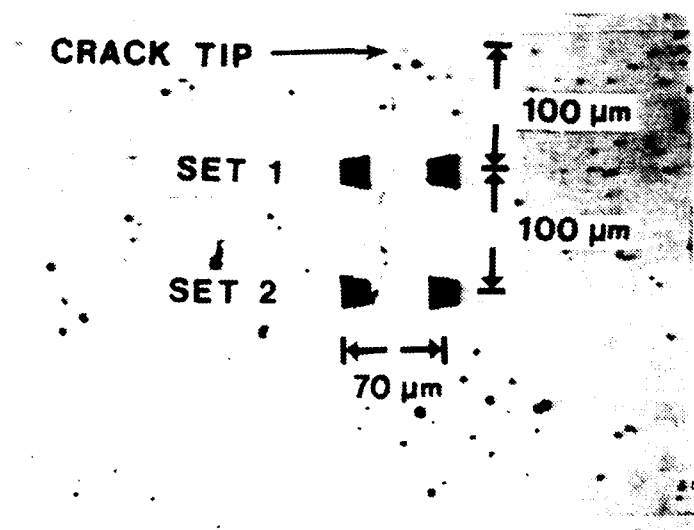


Figure 22: Photomicrograph of two sets of indentations to enable angle measurement. Note the skewed shape of the indents caused by the tilting of the diamond indenter.

If there is no rotation of the specimen, then one can measure the CTOD with only one photomultiplier tube. This is a considerable advantage because most oscilloscopes are two-channel, and this would enable the use of the other channel for another signal—from a foil gage for example. In most of the impact tests, the fringe signals from the two PMTs were very nearly identical; however, in some cases, there were slight differences. It is believed that very careful alignment is the key to uniformity of the signals. There is likely to be more rotation in the static and intermediate-rate tests because of motion of the hydraulic ram as it moves up. Two PMTs or photosensors were always used in those tests, and two PMTs were also used for the final high-rate tests. The point here is that a single fringe pattern can be used if one is very careful with the alignment.

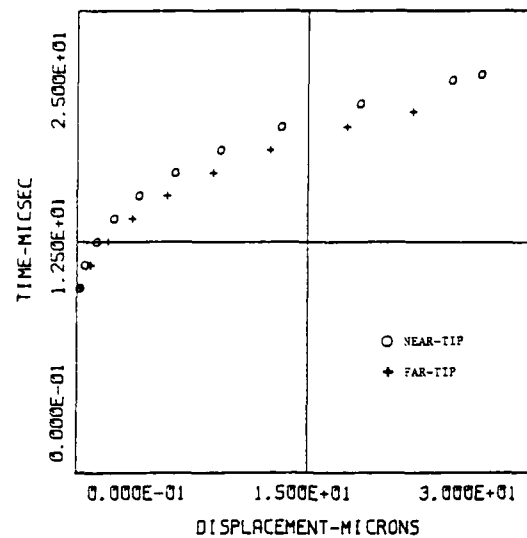


Figure 23: Time versus CTOD from two sets of indents.

The frequency response of the recording system is of course an issue; this is controlled primarily by the load resistor for the PMTs. Figure 24 shows two records from the same test (but two different fringe patterns). One PMT had a 1000 ohm resistor; the other had a 500 ohm resistor. The improvement in frequency response is evident in that the minimums return more nearly to zero. The frequency response with the 1000 ohm resistor is clearly adequate, and that is the value that was routinely used.

## 7.2 Experimental Procedure

The final version of the high-rate test techniques and procedures are presented in this section.

A 3-point bend specimen was impacted by a 25 mm diameter by 150 mm long aluminum projectile fired by a gas gun. The gas gun, which is some 35 years old, has a unique charging and firing chamber with a double-ended piston. The charging chamber is pressurized to the desired pressure and seals one end of the piston. Firing pressure is then applied to the firing chamber where the other end of the piston has a much larger area. When the pressure force on the firing end of the piston exceeds that on the charging end, the piston quickly opens to discharge the charge pressure into the barrel at a high rate. Charging pressures ranging from 60 psi to 100 psi (with firing pressures that are approximately 1/4 that value) are used to produce projectile velocities from 32 m/s (105 ft/sec) to 45 m/s (150 ft/sec).

The 150 mm long aluminum projectile has a blunt nose, and it impacts a hardened steel tup that is initially placed in contact with the specimen. The tup has a wedge-

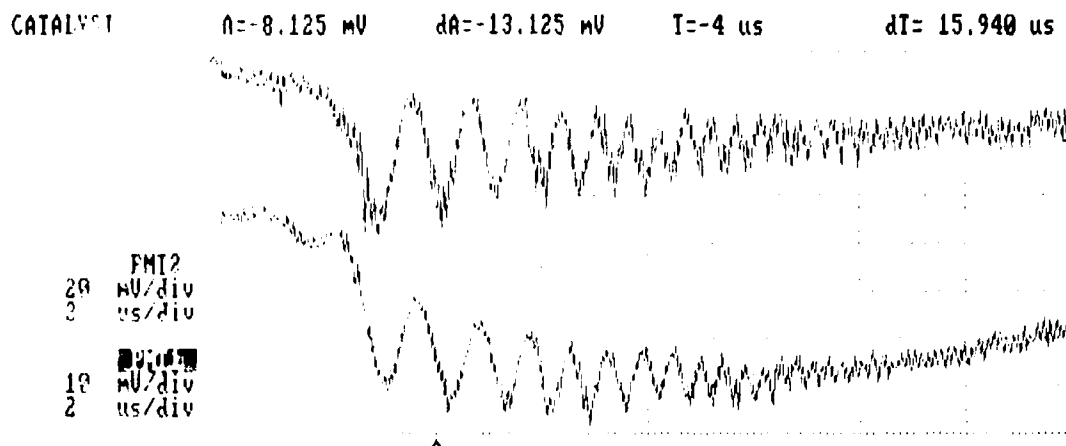


Figure 24: Two fringe intensity versus time traces showing the effect of a smaller load resistor. The load resistor for the upper trace is 500 ohms; for the lower, 1000 ohms.

shaped end lined up with the notch and crack in the specimen and is supported in a Teflon mount. Figure 25 presents a schematic of the setup; the specimen sits on a horizontal steel plate placed in front of the gun, and the Teflon mount holding the tup also sits on this plate.

Figure 26 is a photograph of the setup. The aluminum projectile can be seen protruding from the gun muzzle, and the white Teflon holder sits in front of it. The polished specimen is hard to see as it reflects the black surroundings. The wooden catch-box is lined with high-density styrofoam. The laser sits behind the vertical steel plate and is directed down to the specimen by the steering mirror mounted on the L-shaped rod. Two photomultiplier tube housings are also visible. Amplifiers that were used with foil strain gages in some tests are in the rack at the lower left (along with some unrelated equipment), and a small portion of the LeCroy oscilloscope is visible in the upper lefthand corner.

Fringe motions were recorded by two RCA model 8645 photomultiplier tubes (PMTs) connected to a LeCroy model 9400 digital oscilloscope. The PMTs were powered at 1200-1300 volts by a Power Designs model 1570 high voltage supply. The oscilloscope was triggered in the DC mode internally from either the first fringe signal or a much larger signal that occurred after the specimen was broken and the incident laser beam reflected momentarily into the PMT; this reflection comes from the dimpling of the specimen ahead of the crack tip. Figure 27 is a plot of an entire trace; the 9400 oscilloscope stores a record that is 320  $\mu$ s long with 20 nanoseconds between data points regardless of the sweep speed settings (as long as they are less than 50  $\mu$ s per division). This gives one



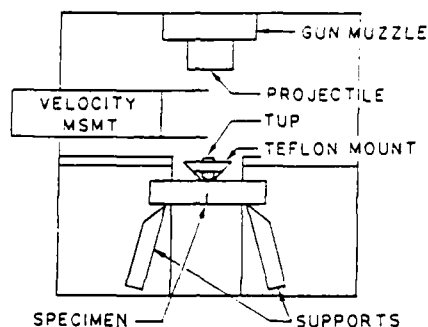


Figure 25: Schematic of the impact test setup.

tremendous leeway in the exact trigger time while preserving the time resolution and is a powerful feature of digital oscilloscopes.

After a test, the contents of the memory of the 9400 are transferred to the IBM/AT through a GPIB interface. They are plotted on the screen for examination using CATALYST software which is available from LeCroy. The pointer in the CATALYST is used to locate the maxima and minima, and these values are written into a file for conversion into CTOD versus time data.

Projectile velocity was measured by two wires spaced 25 mm apart and connected to a resistance divider network and a 6 volt battery. When the projectile hits the first wire, 3 volts appears across the output, and when it hits the second wire, 6 volts appear. These voltages, which are really noisy spikes instead of step functions because the wire doesn't remain in continuous contact with the projectile, are recorded on a Phillips model PM3302 digital oscilloscope. The time between spikes is measured directly from the oscilloscope and converted into velocity. The relative uncertainty of the velocity measurement is estimated as  $\pm 6$  percent with equal contributions from the uncertainties associated with the wire spacing and the time measurement.

Figure 28 shows the two PMT signals from a test on tungsten (Test 52). They have been shifted along the time scale and expanded with the CATALYST software. These records are processed to locate the max/min and converted to CTOD-time plots as shown in Figures 29 to 32

Note in those figures the short duration of the actual deformation. The start of the CTOD is arbitrary because of the uncertainty associated with the trigger. The relative uncertainty in the value of CTOD is estimated at  $\pm 3$  percent and arises entirely from

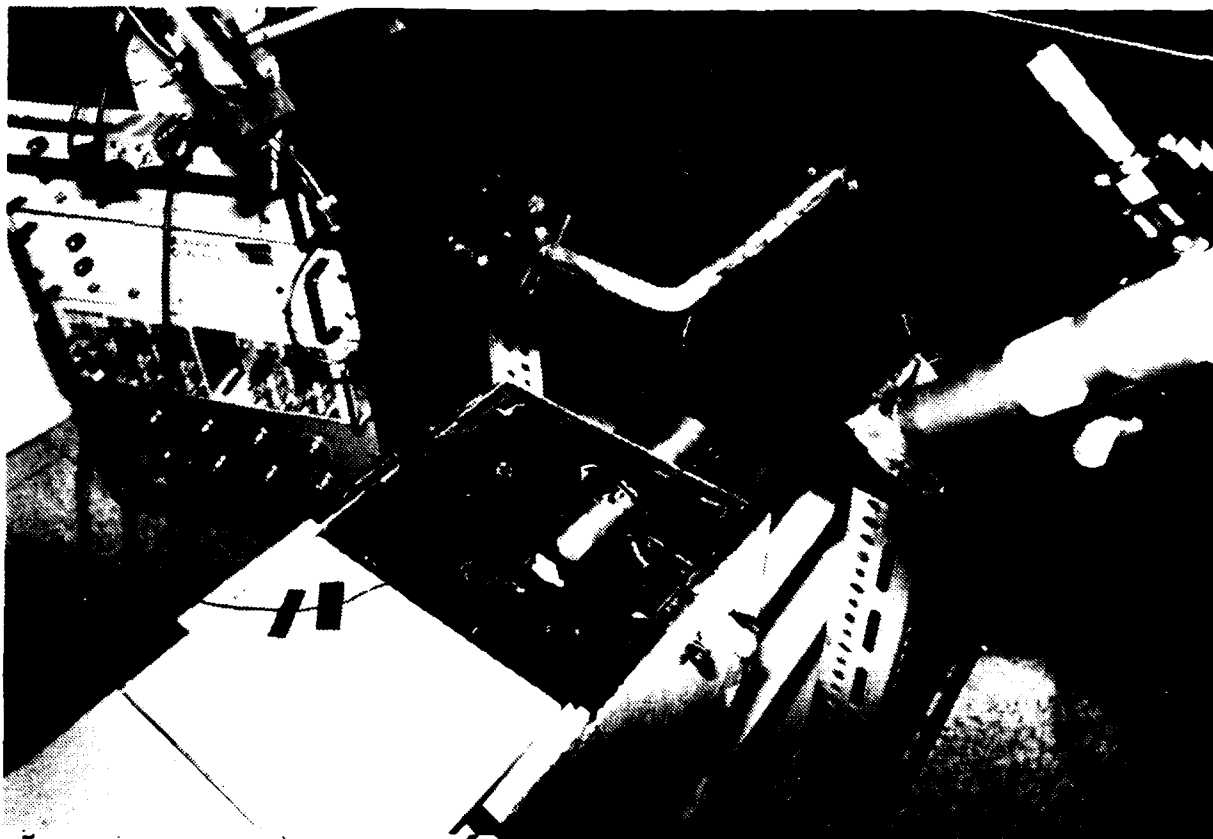


Figure 26: Photograph of the muzzle end of the gas gun showing the specimen, projectile, tup holder and photomultiplier tubes.

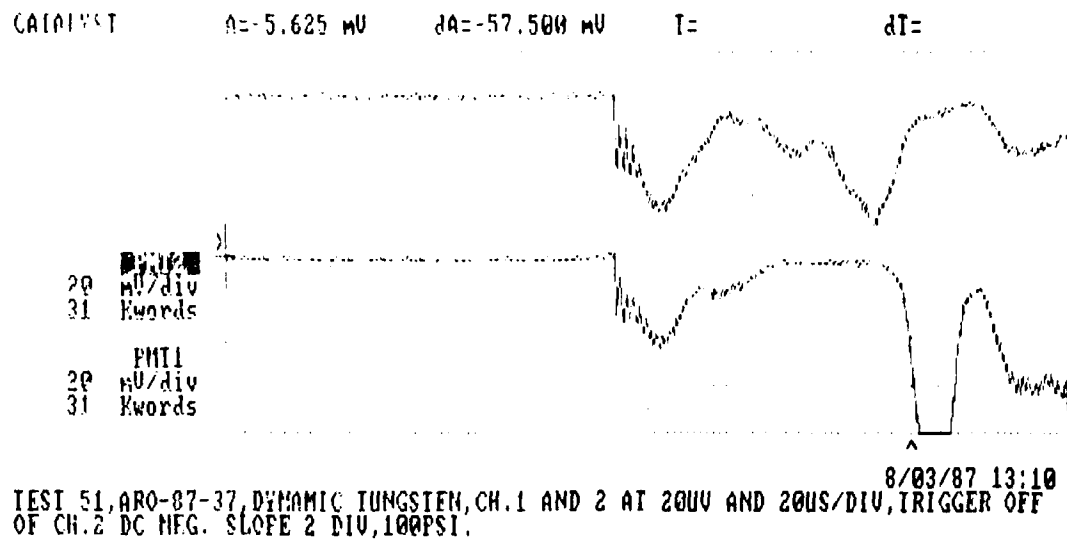


Figure 27: A total fringe intensity versus time trace covering 320  $\mu$ s . The memory triggered at 260  $\mu$ s as indicated by the "A" above the date. The CTOD fringes begin at  $\sim$  145  $\mu$ s .

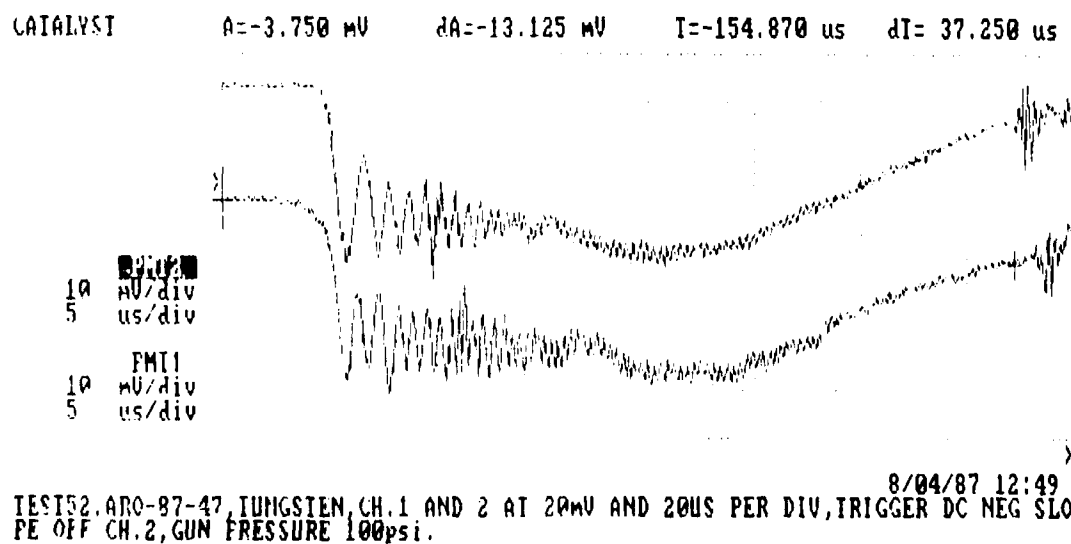


Figure 28: Fringe intensity versus time traces for an impact test.

the measurement of the angle  $\alpha_0$  in the test setup. Measurement of two sides of a triangle is made with a steel scale to determine the angle. The uncertainty in time is estimated at  $0.05 \mu\text{s}$  and is caused by the lack of precision in locating a maximum or minimum on the fringe intensity record.

### 7.3 CTOD versus Time Results

Figures 29–32 present the CTOD-time plots for the four materials. The time has been shifted to a common zero by extrapolating back through the first few max/min to determine the point at which the first deviation of the PMT signal occurred. Note the reproducibility of the data and the fact that in every case, most of the deformation occurred within  $10 \mu\text{s}$ . The SAE-01 specimens were impacted at 33 m/s, and the other materials at 45 m/s.

Figure 29 presents two tests on tool steel that were performed slightly differently. The specimen in Test 39 was not supported horizontally at its ends as were the rest of the dynamic specimens. The specimen was just resting on the plate following the same approach as Giovanola [8]. In view of the short time scale of the test, it is not surprising that the local CTOD responses are very nearly identical.

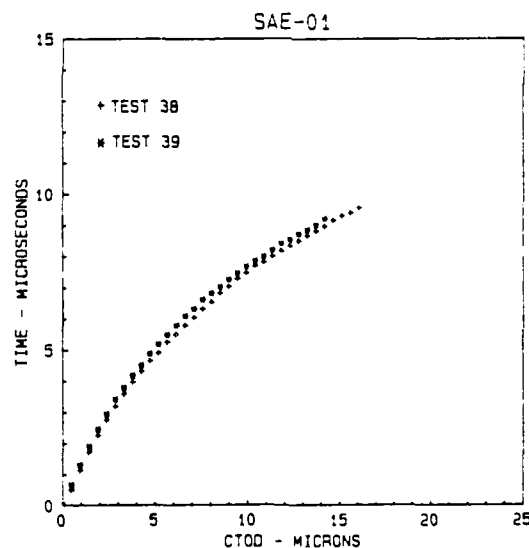


Figure 29: Time versus CTOD plots for two impact tests on SAE-01 steel.

### 7.4 Linearity of the Load Pulse

The CTOD-time plots are valid measurements of the crack-tip-opening displacement as a function of time at the particular position  $100 \mu\text{m}$  behind the crack tip. As such,

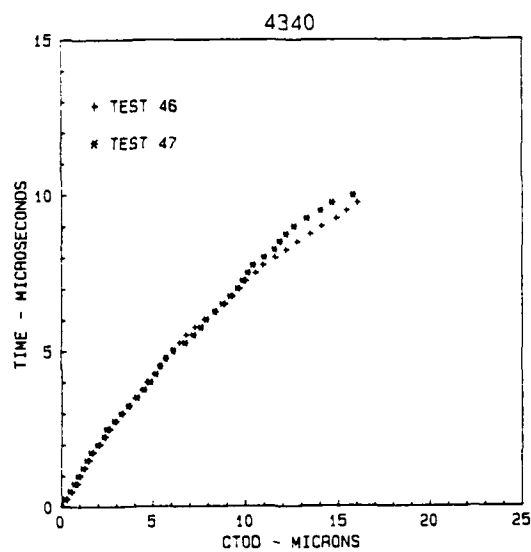


Figure 30: Time versus CTOD plots for two impact tests on 4340 steel.

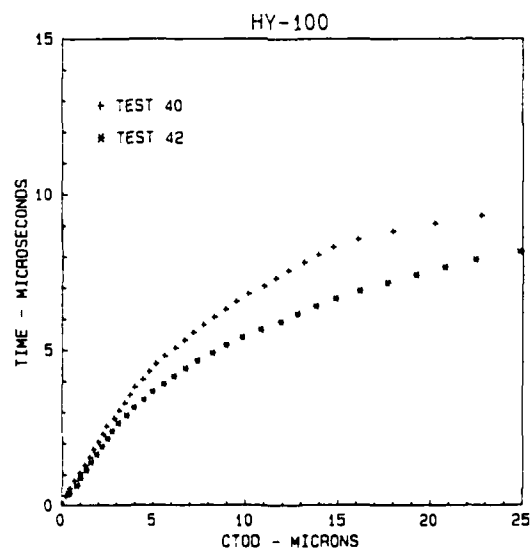


Figure 31: Time versus CTOD plots for two impact tests on HY-100 steel.

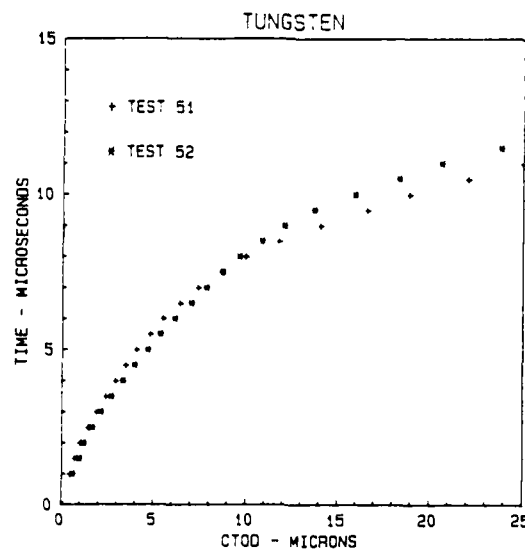


Figure 32: Time versus CTOD plots for two impact tests on tungsten.

they can be used as the input to a finite element program which simulates the behavior of the specimen and enables one to extract various outputs such as stresses at particular points,  $J$ -integral values, etc. But, the CTOD-time results would be more useful if they could be converted to load-CTOD results which would permit a more direct, and easier, comparison with traditional E-399 testing. This can be easily done if the load applied to the specimen increases linearly with time. The first portion of the CTOD-time plot in Figures 29 through 32 indicates that the load is increasing linearly with time; that linear region corresponds to elastic behavior of the specimen—see the corresponding behavior in Figure 12. Whether the load continues to increase linearly after the specimen begins to undergo plastic deformation is another question, but the following two arguments support that assumption.

#### 7.4.1 *Tup Strain Measurements*

Figure 33 is a photograph of the LeCroy 9440 oscilloscope display taken for one of the developmental tests on SAE-01 before the interface to the IBM/AT. The upper trace is from one of the PMTs and shows poor definition of the fringes (it was later learned that an aperture mask inside the tube assembly had shifted). However, the upper trace does show where the fringes occur; they are observed in the first 10–15  $\mu\text{s}$  of the trace. The rest of the trace shows the reflection of the laser beam into the PMT. The lower trace is from a foil strain gage attached to the tup. Although the signal is noisy and is clipped, it does return to the initial zero after the pulse has passed. The important point is the generally linear rise in the pulse during the first 10  $\mu\text{s}$ . This test was run at the same firing pressure as the one shown in Figure 29, so almost all of the measured CTOD had

occurred within  $10 \mu\text{s}$ . So, the input pulse, as measured on the tip, increases in a linear fashion for times longer than required for local plastic CTOD.



Figure 33: Fringe intensity (upper trace) and strain on the tip (lower trace) for an impact test.

#### 7.4.2 Finite Element Analysis

Dynamic finite element calculations (the essential points of which are summarized in section 8, with computational details and results given in appendix A) show that the component of stress which acts to open the crack increases almost linearly with time. There is an initial small short compressive pulse followed by a small but sharp tensile pulse of  $\sim 2 \mu\text{s}$  in this stress component which is computed about 0.8 mm away from the crack. Thereafter it rises linearly with time.

### 7.5 Load versus CTOD Results

In order to compare the response of a material for various loading rates, there must be some common measure, and this is the local load-CTOD plot. This plot is directly recorded in the cases of the static and the intermediate-rate tests, but it must be computed indirectly in the impact case (as it is by every other technique for measuring dynamic fracture toughness). Based on the assumption of a linearly increasing dynamic load past the point of crack initiation (as discussed in the previous section) and noting that the crack lengths and position of the indents behind the tip are nearly the same for all specimens, the dynamic load-CTOD plot is generated as follows:

1. Measure the initial linear slope of load versus CTOD in the static case.
2. Measure the initial linear slope of time versus CTOD in the dynamic case.
3. Use the results from steps 1. and 2. to compute a conversion factor with units of  $\text{N}/\mu\text{s}$  and change the time scale in the dynamic tests to a load scale.
4. Use the previously measured (before the specimen was impacted) value of the closure load to establish the load at which the CTOD begins to increase.

Steps 1-3 scale the ordinate of the plot, and step 4 sets the intercept at zero CTOD.

The slopes in these conversions were obtained by drawing straight lines on the plots; a more sophisticated numerical approach could be used. The static slopes (step 1) for SAE-O1, 4340, and HY-100 were 319, 360, and 319  $\text{N}/\mu\text{m}$  respectively; they are nearly equal as they should be since the geometry and elastic modulus are the same. The slope for tungsten is higher at 570  $\text{N}/\mu\text{m}$  since the elastic modulus is higher. The dynamic slopes (step 2) for SAE-O1, 4340, and HY-100 were 1.2, 1.0, and 0.88  $\mu\text{s}/\mu\text{m}$  respectively; the slope for tungsten was also 1.2  $\mu\text{s}/\mu\text{m}$ .

Closure loads were measured before every dynamic test on each specimen by placing them in the setup used for static tests and increasing the load carefully until the fringes had moved one-half unit, i.e. dark to bright. The first half fringe in a dynamic test was then assigned this value of closure load (step 4). This is well within the region of elastic behavior and is an important part of the procedure.

The relative uncertainty in the CTOD is  $\pm 3$  percent as before. The relative uncertainty in the load must include the uncertainties in the static and dynamic slopes in steps 1 and 2. Assuming that one can measure these slopes within  $\pm 3$  percent, the total relative uncertainty for a load measurement is 6 percent plus 0.05  $\mu\text{s}$  (uncertainty in time) divided by the time corresponding to that load.



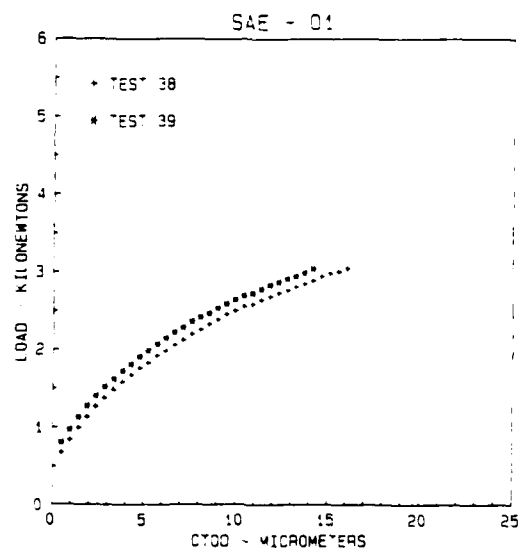


Figure 34: High-rate Load - CTOD plots for SAE-O1

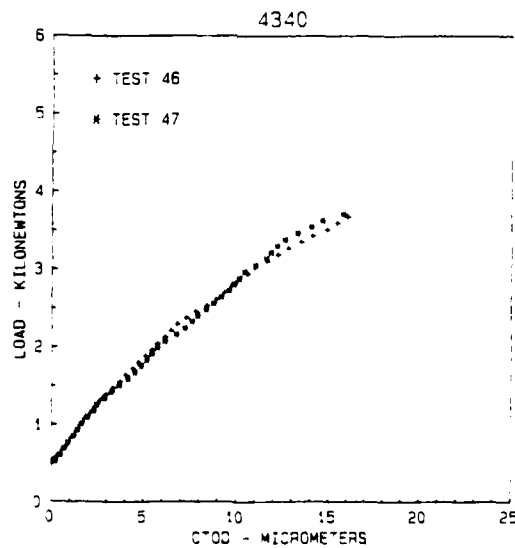


Figure 35: High-rate Load - CTOD plots for 4340

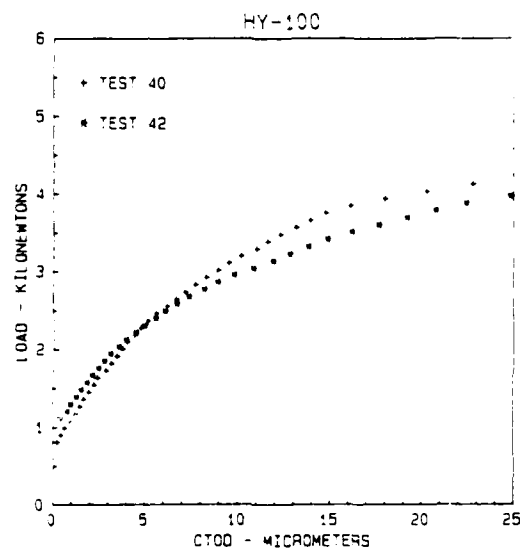


Figure 36: High-rate Load - CTOD plots for HY-100

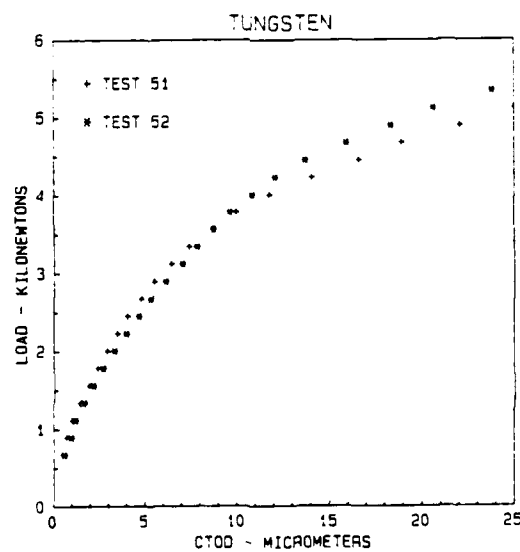


Figure 37: High-rate Load - CTOD plots for tungsten

## 8 Finite Element Computations

### 8.1 Introduction

The static and dynamic fracture experiments have been complimented by a series of finite element calculations which simulate the behavior of the three point beam specimen. These calculations reflect as accurately as possible the specimen geometry, material behavior and loading conditions corresponding to the performed experiments. Since the focus of this report is on the static and dynamic fracture *experiments*, the details of the finite element computations appear in Appendix A. A brief summary of procedures and results is given here.

All the calculations were done using the advanced non-linear finite element code ABAQUS (distributed by Hibbitt, Karlsson and Sorensen, Inc. Providence RI), which has been used for similar calculations, for example by Nakamura *et al.* [48,49]. Most of the computations were done on the Mechanical Engineering MicroVAXII, while a few were done on the CRAY XMP at the Naval Research Laboratories, Bethesda, MD.

Since the fatigue precracking procedure produces initial crack lengths which are not completely uniform, each mesh is adjusted to produce a crack of the correct length. The *initiation* toughness is of primary interest here, all calculations were done for a *stationary* crack (no growth law was incorporated). However, the release of several nodes was used to simulate the actual crack initiation behavior for the static analysis of 4340 steel. In all cases the crack is assumed to be mathematically sharp. Small deformation theory is used throughout.

### 8.2 Static Calculations

For the static tests, the specimen is simulated by two-dimensional plane stress and plane strain elements. Most of the specimen is modeled by plane stress elements, while a small area near the crack tip (the radius of this region is about 10%-30% of the specimen thickness) is modeled using plane strain elements. This combination of plane stress and plane strain deformation effectively allows a 2-D calculation to simulate 3-D effects—with the accompanying economy in the calculations—and has been used to good effect before by Newman [50,51] and corresponds reasonably with the experimental evidence reported by Rosakis and Ravi-Chandar [52]. Two eight-node plane strain isoparametric elements with the mid-side nodes placed at the quarter points closest to the crack tip are used around the crack tip. This technique effectively simulates the elastic singularity for purely elastic deformation [53]. The static calculation used only a graded mesh, which has elements on the order of  $\sim 35 \mu\text{m}$  in the neighborhood of the crack and elements on the order of 1 mm away from the crack, supports and loading. Only the one half of specimen itself need be modeled due to symmetry.

For quasi-static loading, the loads and supports are modelled as a point load (on

a node with local mesh refinement) which is increased monotonically and fixed (zero displacement) supports, respectively.

The material stress versus strain laws, as given in Section 4, are modeled as isotropic hardening, multi-linear, elasto-plastic materials using a von Mises yield criterion. The engineering 0.2% offset stress is not used as the yield stress—the onset of plasticity is taken to occur at the end of the linear region of the stress versus strain curve, see Figure 3.

### 8.3 Dynamic Calculations

In the dynamic tests, inertia plays a major role, and the combination of plane stress and plane strain elements may lead to undesirable stress wave reflections and impedance mismatch at the plane stress/plane strain interface. Therefore plane stress elements were used throughout.

Two specimen meshes were used for the dynamic calculations—a graded mesh with an element size on the order of  $35\ \mu\text{m}$  near the crack tip and a uniform mesh with a nearly uniform mesh size of 1 mm. Since the dynamic loading is a function of the interaction of the projectile, tup and specimen, all three components must be modeled in the finite element simulation. Dynamic calculations therefore included the projectile (with an initial velocity), tup and specimen. The graded mesh model for the specimen used four-node quadrilateral finite elements in combination with 18 eight-node elements surrounding the crack tip. For the tup and projectile, only four-node quadrilateral elements are used. Elements of different thickness are employed to model the cylindrical geometry of both the tup and projectile. Plane stress is assumed for the finite element modelling of the specimen and the tup, while plane strain is assumed for the projectile. This is because the bulk of the projectile (which is cylindrical) act in manner more like plane strain. than plane stress. Both the graded and uniform meshes for the specimen were used in the dynamic calculations. The graded mesh model was used to give CTOD versus time information, while the uniform mesh model was used to check that the graded mesh model did not give poor results because of possible wave reflections and impedance mismatch at the interface between large and small elements.

The impact of the projectile (which has a mass greater than 5 times the mass of the tup and specimen combined) with the tup and specimen is modeled by giving the projectile the experimentally measured velocity for that experiment. Tup and specimen begin with zero velocity. Impact is assumed to be perfect and normal.

The impact initiation process is completed in less than  $20\ \mu\text{s}$  and the deformation is therefore considered to be adiabatic. Since our main concern is the displacement field near the crack tip in the first 10 to  $20\ \mu\text{s}$ , the friction between the specimen and the tup and the specimen and the supports is ignored.

The dynamic behaviour of materials is very complicated and only very restricted

amount of data is available for some materials. However, viscoplastic effects are very important in these calculations and a flow-stress versus strain-rate material law of the type [54,55,56]

$$\dot{\epsilon}^p = D (\sigma/\sigma_0 - 1)^P \quad \text{for} \quad \sigma \geq \sigma_0 \quad (8.1)$$

is used for the dynamic calculations. Here,  $\sigma$  is the effective yield stress at a nonzero strain rate,  $\sigma_0$  is the static yield stress (which may depend on the equivalent plastic strain,  $\epsilon^p$ , via isotropic hardening), and  $\dot{\epsilon}^p$  is the plastic strain rate. The flow stress  $\sigma_0$  as a function of plastic strain rate  $\dot{\epsilon}^p$  is plotted as a function of the material parameters  $D$  and  $P$  in Appendix A.

The Hilber-Hughes-Taylor (HHT) [61] implicit time integration algorithm, with a fixed time step of  $0.1 \mu\text{s}$  was used. Since the implicit integration scheme is stable, this allows for larger time increments. Equilibrium tolerance (parameter PTOL) is required for implicit integration. All forces at all nodes must fall below this tolerance for the solution to be accepted. Usually PTOL is set to a small fraction ( $10^{-2}$  to  $10^{-4}$ ) of typical actual force values. A small amount of damping is provided for by setting the HHT parameter  $\alpha = -0.05$  which removes the high frequency oscillations. An examination of the energy balance shows that this damping does not cause more than an insignificant amount of dissipation. For a discussion of implicit time integration schemes for the impact response of structures, see Belytschko [63].

The displacement at the indent position (i.e.  $0.1 \text{ mm}$  behind the crack tip and  $0.035 \text{ mm}$  from the crack edge) is output on file every  $1 \mu\text{s}$  and retrieved during post-processing to be plot as the curve of CTOD vs time for each computational simulation.

For a typical run, the stress fields of selected elements near crack tip are output about every  $1 \mu\text{s}$ . This is done to check the validity of computation model and material behavior. The results also confirm that the local stress field rises linearly (see section 7.4.2).

## 9 Discussion of Results

It is useful to plot the load versus CTOD results for the static and the dynamic tests on the same plot. This is done for the four materials in this section, and the dynamic values of  $P_q$  are determined.

### 9.1 Static and Dynamic Load versus CTOD plots

Since the closure loads for the various static and dynamic specimens were different, it is necessary to shift the curves to a common origin. Linear behavior is observed in all cases for an initial portion of the recorded load-CTOD, and it is reasonable to assume that the behavior would have been linear beforehand if there had been no closure. It is therefore appropriate to "draw in" the initial portion of the load-CTOD plot beginning at "zero-zero" by using the same slope that was measured after the closure load had been exceeded.

An average slope for each material was used to draw the initial portion of the plots. These slopes were the same one used in constructing the dynamic curves i.e.  $319 \text{ N}/\mu\text{m}$  for the SAE-01,  $360 \text{ N}/\mu\text{m}$  for the 4340,  $319 \text{ N}/\mu\text{m}$  for the HY-100, and  $570 \text{ N}/\mu\text{m}$  for the tungsten. The static data plotted in Figures 12 through 15 is replotted in Figures 38 through 41. The dynamic data from Figures 34 through 37 is also replotted there.

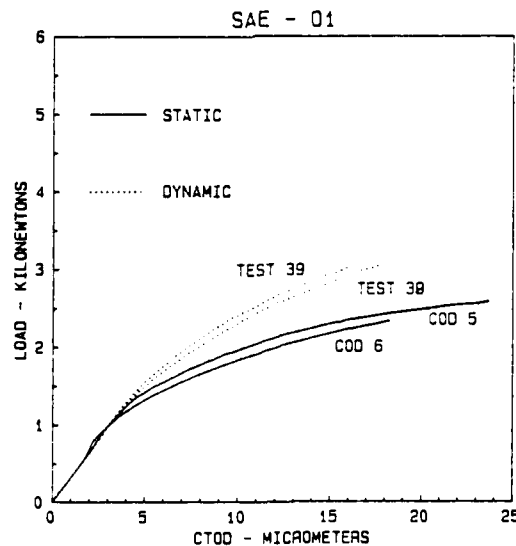


Figure 38: Final static and dynamic data for SAE-01 steel

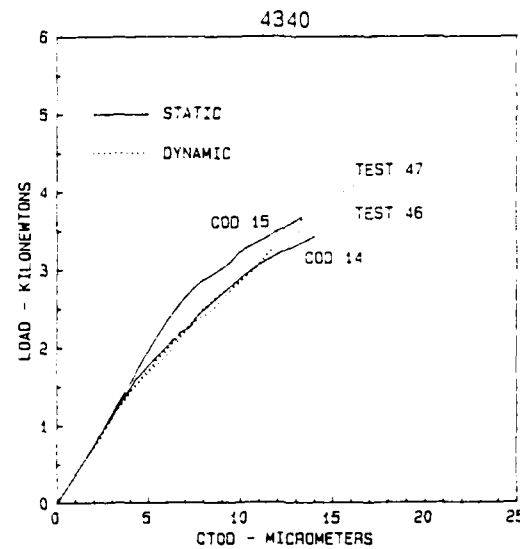


Figure 39: Final static and dynamic data for 4340 steel

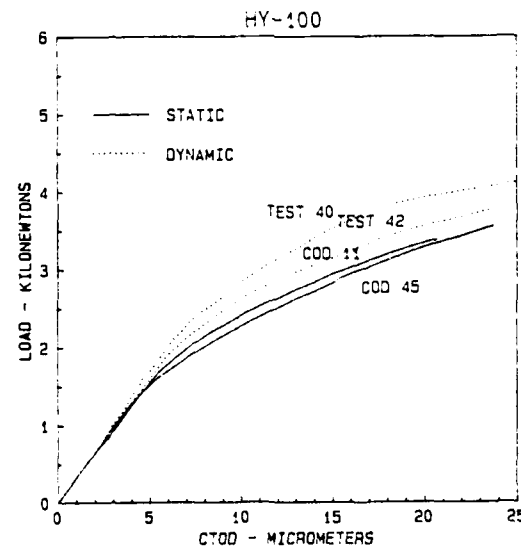


Figure 40: Final static and dynamic data for HY-100 steel

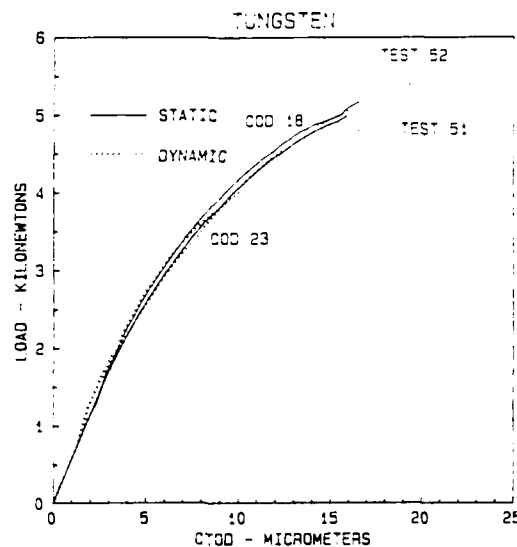


Figure 41: Final static and dynamic data for tungsten

## 9.2 Critical Loads for the High-Rate Tests

The critical loads for the static tests were established from the clip gage data using the ASTM E-399 procedure. These loads can be used in conjunction with the static load-CTOD data to establish a "reduced slope" for a load-displacement plot measured near the crack tip. This is analogous to the reduced slope used in ASTM E-399 (5 percent reduction) except that it is measured at a different position on the specimen. Assuming this geometrical construction which purports to identify the onset of crack propagation is independent of loading rate, one can then use the local reduced slope to determine the  $P_q$  from the dynamic load-CTOD plots.

The approach taken here to establish the critical loads  $P_q$  for the high-rate tests is as follows:

1. Plot the static  $P_q$  on the static load-CTOD plot.
2. Draw a secant line from the origin to that point.
3. Measure the slope of the secant line.
4. On the dynamic load-CTOD plot, draw a secant line with the same slope and read the dynamic  $P_q$  where it intersects the curve.

This procedure requires that the crack lengths and indentation locations be as nearly identical as possible for all the specimens at the different loading rates. It does not require that the closure loads be the same as long as a sufficient linear region is recorded



at the beginning of the load-CTOD plot; however, it is highly desirable that the pre-cracking procedures be similar. The procedure can actually be done on a single plot that contains both the static and the dynamic data. Figures 42 - 45 show this for the four materials.

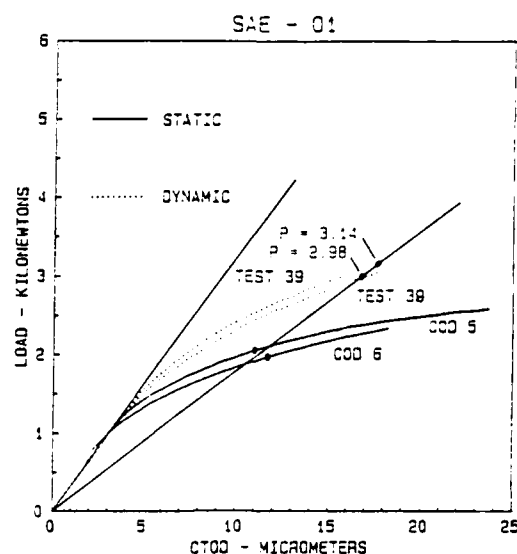


Figure 42: Determination of dynamic  $P_q$  for SAE-01

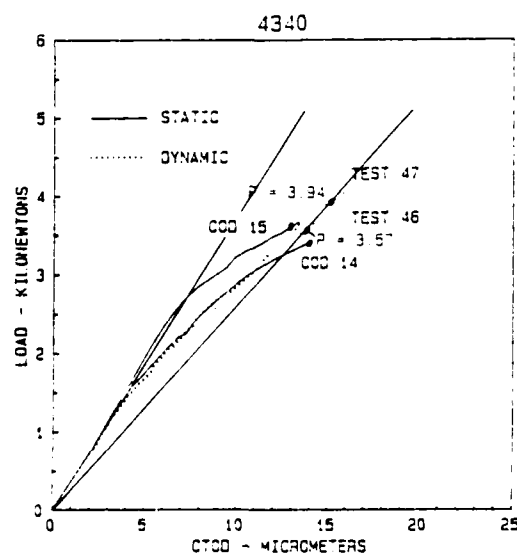


Figure 43: Determination of dynamic  $P_q$  for 4340

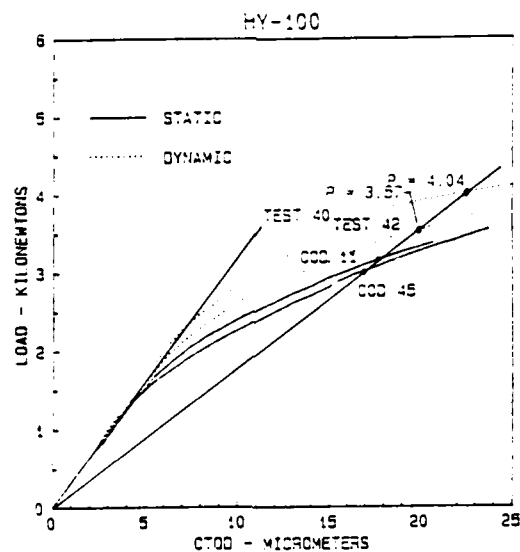


Figure 44: Determination of dynamic  $P_q$  for HY-100

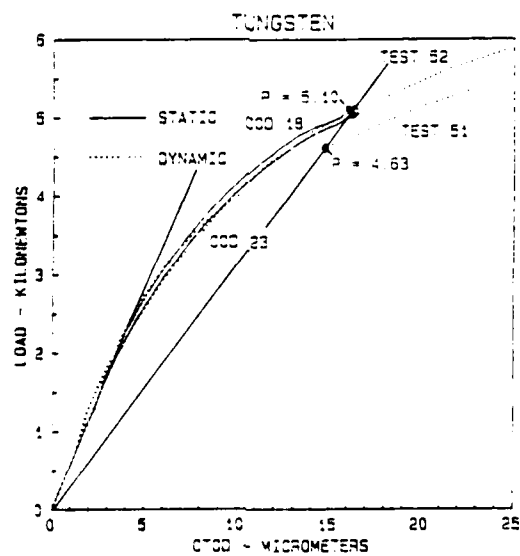


Figure 45: Determination of dynamic  $P_q$  for tungsten

The static values of  $P_q$  are plotted as points on the static CTQD curves, and an average slope is drawn. In all cases except the 4340 steel, the static slope is nearly identical for the two specimens. The intersection of this local CTOD slope with the dynamic CTOD curves is taken as the measure of the dynamic  $P_q$ , and these values are labelled on the plots. The  $P_q$ s obtained are slightly different because the local CTOD response of each specimen is different.

The original elastic slopes are also drawn on Figures 42 - 45 so that a comparison may be made between them and the slope of the line to the  $P_q$ . The ratio of the  $P_q$  slope to the elastic slope is 0.55 for SAE-01, HY-100, and tungsten, and is 0.7 for the 4340 steel. These values contrast with the 0.95 that is used in E-399. Of course, the slopes would be different if the indentations were located at a different position behind the crack tip.

Table VI

Material	Static $K_q$ MPa $\sqrt{m}$	High-Rate $K_q$ MPa $\sqrt{m}$
SAE-01	31.2	49.0
	35.2	51.6
4340	51.0	55.9
	58.9	63.0
HY-100	49.9	65.5
	58.5	61.5
tungsten	63.0	68.8
	62.5	75.8

The only material that has been tested extensively is the 4340 steel. Costin et al [5] measured static/dynamic values of 62/55.6 MPa $\sqrt{m}$  for 4340 with a  $R_c$  of 48. Giovanola [8] tested a slightly harder material ( $R_c = 50$ ) and measured static/dynamic values of 64-65/52-63 MPa $\sqrt{m}$ . The results reported here give similar values for a 4340 steel with  $R_c = 52$ , but show a tendency for the  $K_q$  to remain constant or increase slightly with rate (one really can't draw a conclusion on such limited data). In any event, comparison of the dynamic  $K_q$  measured with this technique shows good agreement with other techniques.

The SAE-01 tool steel shows a clear and significant increase in  $K_q$  with rate—as does the HY-100. Couque et al [69] studied a low carbon steel subjected to various heat treatments and measured the dynamic  $K_q$  with the annular-rod technique at Brown University. In every case, they found that at higher temperatures where the material is more ductile, the dynamic  $K_q$  was larger (as much as 50 percent in one case) than

the static value. The results obtained here for these two very ductile materials are consistent with their measurements.

Little information exists on tungsten, so no comparisons are possible. The results obtained here show essentially no effect of the loading rate.

### 9.3 Fracture Surfaces

Figures 46 - 49 are macrophotographs of fractured specimens--one from each material. In each case, the dynamic specimen is on the left. The SAE-01 dynamic specimen shows the familiar "river" patterns emanating from the crack. There is more deformation of the loading side of the specimen than there is in the static case. Although the surfaces themselves appear different in the photo, examination at higher magnification with an optical microscope shows the structure to be essentially the same.

The 4340 steel specimens look the same although there are slightly larger shear lips on the static one. Note the deformed region on the back of the specimen where the tup indented it.

The HY-100 is a very tough material, and this is evident in the large deformation seen in Figure 48. Again, there is little difference between static and dynamic appearances.

The crack front in the tungsten specimens was essentially straight, although it is very hard to define. The material exhibited a brittle behavior with very little shear, and the dynamic and static appearances are the same.

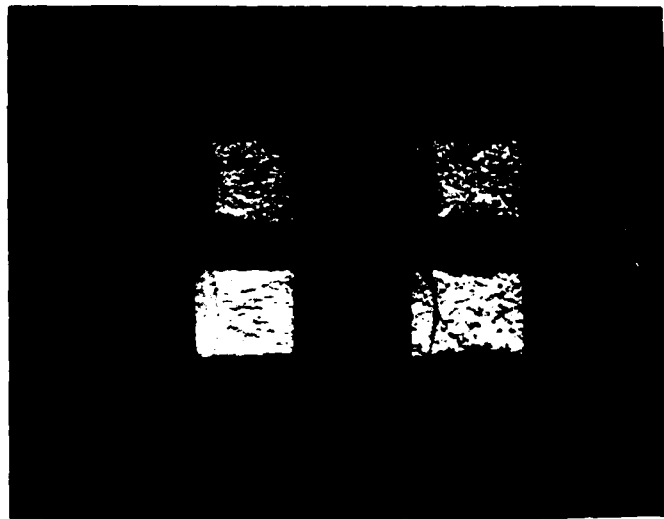


Figure 46: Fracture surfaces of SAE-01 steel; the dynamic specimen is on the left.

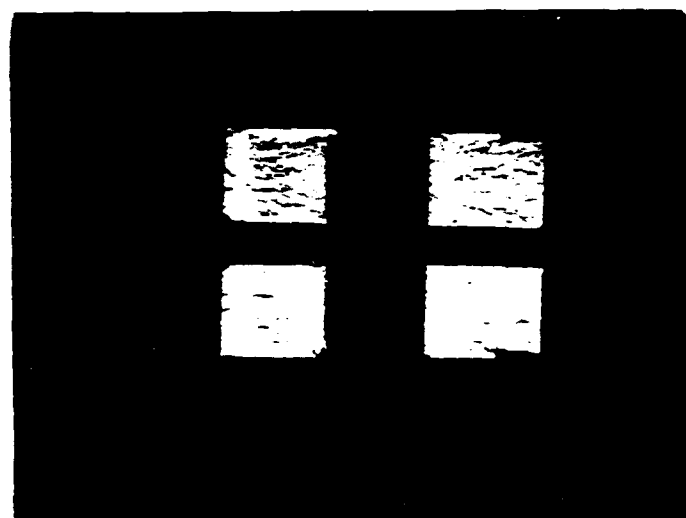


Figure 47: Fracture surfaces of 4340 steel; the dynamic specimen is on the left.

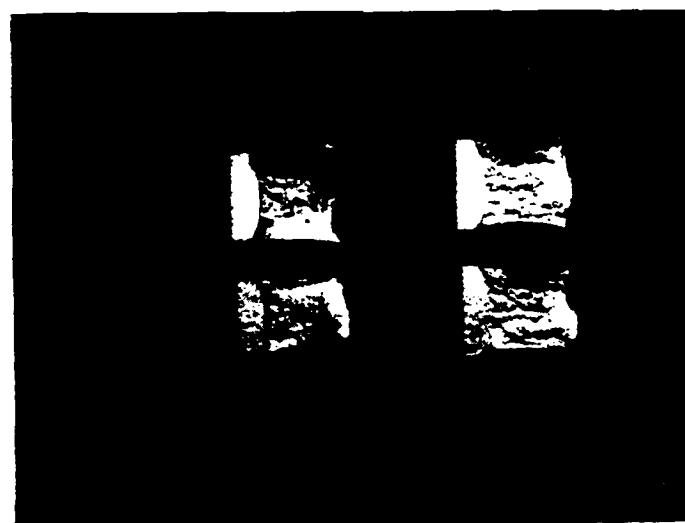


Figure 48: Fracture surfaces of HY-100 steel; the dynamic specimen is on the left.



Figure 49: Fracture surfaces of tungsten; the dynamic specimen is on the left.

#### 9.4 Uncertainties of Measurement

The uncertainties in the final value of a  $P_q$  of course depend on the uncertainties associated with both the static and the dynamic load versus CTOD data. As discussed in the earlier sections, the relative uncertainties of the static load-CTOD data are  $\pm 3$  percent for the CTOD and  $\pm 1$  percent for the load. Three typical points for the HY-100 test number COD 45 are plotted in Figure 50 along with the uncertainty bars, and the mean curve is drawn in.

For the dynamic tests, the relative uncertainties in the load total  $\pm 6$  percent (3 percent from each of the slopes) plus  $0.05 \mu s$  divided by the time. The uncertainty in the CTOD is the same as before. Typical points and the associated uncertainties are plotted in Figure 50 for the dynamic TEST 42 and the bounding curves sketched in.

With these bounding curves, one can proceed to estimate the uncertainty in the final value of  $P_q$ . Assume that the  $P_q$  determined from the clip gage data is uncertain within  $\pm 5$  percent. This would shift the intersection point of the "reduced slope" straight line along the static load-CTOD curve only a little bit. Clearly the major source of variation in the determination of  $P_q$  comes from the variation in the dynamic load-CTOD curve.

The value of  $P_q$  from the measured data is 3.57 kN. The  $P_q$  determined by the intersection of the reduced slope line with the upper bounding curve is 3.92 kN; the lower value is 2.90 kN. So, the value of  $P_q$  to be reported is 3.57 kN  $\pm 10$  -20%. The asymmetry in the uncertainty arises from the nonlinearity of the load-CTOD plots.

Based on this analysis, it is therefore reasonable to present the dynamic  $K_q$  values as  $X \pm 10$  -20%.

If this evaluation is applied to the data for 4340 steel, the two measured dynamic values, 55.9 and 63.0  $\text{MPa}\sqrt{\text{m}}$ , could represent a range from 44.7 to 69.3  $\text{MPa}\sqrt{\text{m}}$ . Costin et al [5] reported a single value for 4340 of 55.6  $\text{MPa}\sqrt{\text{m}}$  with no discussion of the measurement uncertainty. However, Couque et al [69], in a more extensive series of tests on another steel using the same technique, reported scatter on the order of  $\pm 10\%$  for both static and dynamic tests. For example, 8 static  $K_{Ic}$  tests at room temperature produced the value  $70 \pm 8 \text{ MPa}\sqrt{\text{m}}$ . Giovanola [8] reported 6 data points for 4340 ranging from 52.0 to 63.6  $\text{MPa}\sqrt{\text{m}}$ . It is not clear in any of these studies whether the variation arises from the measurement technique or the material and specimen differences.

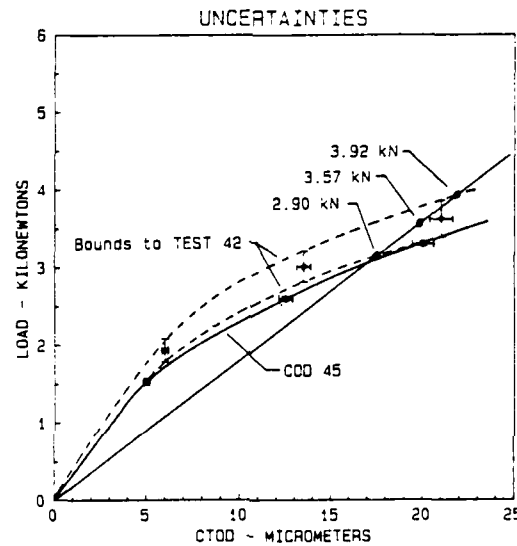


Figure 50: Uncertainties in determining  $P_q$

## 10 Conclusions

The laser-based ISDG is a useful technique for measuring the local crack opening displacement directly behind the tip of a crack. All measurements were made at a position 100  $\mu\text{m}$  behind the tip of the fatigue precrack, and the results were reproducible from specimen-to-specimen. The static setup is quite easy to use, and the intermediate-rate and impact measurements are only slightly more sophisticated. The ISDG measurements of the CTOD can be regarded as valid within  $\pm 3$  percent whether they are taken as a function of load or time. The interpretation and use of the data is less straightforward since these near-tip measurements are relatively new—especially in the dynamic case. However, the response of a cracked structure or component is dependent upon the behavior at the crack tip, and that is where the measurements should be made.

In the static tests, where one can compare the local behavior (CTOD) with clip gage results (CMOD), the identification of crack extension from the CTOD data is difficult because of the large amount of plasticity surrounding the crack tip. It is difficult to separate the plasticity from the crack extension; in a CMOD plot the local plasticity in the early stages of loading is masked by the dimensions of the specimen. Just as a reduced slope (5 percent) is used in ASTM E-399 to delineate the onset of crack extension, a larger reduced slope can be used to identify the same point on the CTOD plot. This offers the opportunity to determine critical loads in specimens under difficult environmental conditions where a clip gage cannot be used or on actual components or structures.

The intermediate rate tests (loading time on the order of 50 ms) in a regular electrohydraulic test machine were inconclusive. The fact that the deformation at the tip, as measured by the ISDG, starts before either the clip gage or the load cell signal changes indicates that wave effects may come into play even in a moderately fast test. Further testing in which tests are run in exactly the same manner, but at various rates, are needed to settle this issue.

The dynamic ISDG measurements of the CTOD as a function of time are also valid within  $\pm 3$  percent. They show an initial linear region, where the local crack tip fields are governed directly by the elastic stress intensity factor. In effect, one therefore has a "K gage". If the loading rate under dynamic conditions is constant during the linear part of the CTOD-time response, then it is possible to convert this CTOD-time information to load-CTOD data since both static and dynamic loading conditions give rise to identical local crack tip fields characterized by the stress intensity factor. If it is further assumed that the loading rate is essentially constant to the point of crack initiation, the dynamic CTOD-time data can be converted into load-CTOD data, which can be analysed in a manner similar to the static data which is based on the ASTM E-399 procedure. However, the additional step in producing the load-CTOD data add to the uncertainty, leading to a relative uncertainty of the load of  $\pm 6$  percent.



The assumption that the loading rate is constant is validated from strain measurements on the loading tup (which rise linearly during the experiment) and from dynamic FEM analyses (which show linearly increasing opening stresses). Strain-rate effects do not affect the elastic response of the material, and therefore do not influence the CTOD-time to load-CTOD conversion—which uses the linear (elastic) regions of the static and dynamic tests. Strain-rate effects are reflected in the individual material's response to dynamic loading and plays a significant role in determining dynamic fracture toughness. Note that the load-CTOD data for 4340, which is a highly rate-independent material, is almost identical for static test COD14 and dynamic tests 46 and 47 in Figure 39. On the other hand, HY-100, which is strain-rate dependent, has clearly different static and dynamic responses (see Figure 40).

The process of drawing a reduced slope on the static load-CTOD plot based on the  $P_q$  obtained via ASTM E-399 and then using that same slope to determine the dynamic  $P_q$  is similar to procedures that have extended E399 to higher rates. Given the assumptions used in the generation of the dynamic load-CTOD curves, this is a perfectly reasonable thing to do. The values of  $P_q$  obtained are subject to a large relative uncertainty—+10 percent and -20 percent—but other test methods show a similar variation. Of the four materials tested, the two very ductile materials showed an increase in  $K_q$  at the high rates, and the two more brittle materials remained essentially unchanged.

The unique feature of these measurements is that they are made at the crack tip; one does not extrapolate from far-field data. Even on this scale there is a question as to what “at the crack tip” means. The indentations were placed 100  $\mu\text{m}$  behind the tip for no other reason than convenience and the fact that experience had showed that the displacement reached a suitable magnitude there. Indentations could just as easily be placed further back or slightly closer. A potential value of the CTOD-time data is that it can be used in a hybrid experimental-numerical scheme, and this approach has been explored in a preliminary fashion here.

Dynamic material property measurements are difficult, and the development of a widely used technique does not come easily—witness the 15 years or more that it took for the Split Hopkinson Bar test to become more or less the standard way of measuring dynamic stress strain curves. This is a different approach that offers some advantages and has some limitations.

The finite element calculations provide a means of assessing the roles of rate sensitivity, inertia and other material characteristics on dynamic fracture initiation. It would be desirable to have sufficient confidence in the computations to use them as the means of establishing the point of initiation. This is difficult because of the nature of the experiments which these computations model. The indents are on the surface and set a length scale of 35  $\mu\text{m}$ . The materials are ductile and rate sensitive. Wave effects dominate since fracture occurs after only about 2 to 3 passes of the elastic shear wave.

However, the computations have been successful in verifying aspects of the experi-

mental procedure. They are able to model the crack tip opening displacement versus time and they provide the essential framework for the understanding of what factors contribute to rate dependent fracture toughness.

## References

- [1] Shoemaker, A.K. and Rolfe, S.T., "The Static and Dynamic Low-Temperature Crack-Toughness Performance of Seven Structural Steels", *Engineering Fracture Mechanics*, pp. 319-339, 1971.
- [2] Rolfe, S.T. and Barsom, J.F., "Fatigue and Fracture Control", Prentice-Hall, 1977.
- [3] Shoemaker, A.K. and Seeley, R.S., "Summary Report of Round robin Testing by the ASTM Group E24.01.06 on Rapid Loading Plane-Strain Fracture Toughness Testing", *J. of Testing and Evaluation*, pp. 261-272, 1983.
- [4] Server, W.L., "Impact Three-Point Bend Testing for Notched and Precracked Specimens", *J. of Testing and Evaluation*, pp. 29-34, 1978.
- [5] Costin, L.S., Duffy, J., and Freund, L.B., "Fracture Initiation in Metals Under Stress Wave Loading Conditions", ASTM STP 627, pp. 310-318, 1977.
- [6] Chevallier, J.M., Ansart J.P., and Dormeval, R., "Fracture Toughness of Some Metals Under High Loading Rate Conditions", *Inst. Phys. Conf. Ser. No. 70* pp. 229-236, 1984.
- [7] Klepaczko, J.R., "Discussion of a New Experimental Method in Measuring Fracture Toughness Initiation at High Loading Rates by Stress Waves", *J. of Engineering Materials and Technology*, pp. 29-35, 1982.
- [8] Giovanola, J.G., "Investigation and Application of the One-Point-Bend Impact Test", ASTM STP 905, pp. 307-328, 1986.
- [9] Ravi Chandar K. and Knauss, W.G., "Dynamic Crack-tip Stresses under Stress Wave Loading - a Comparison of Theory and Experiment", *Int. J. of Fracture*, pp. 209-222, 1982.
- [10] Rosakis, A.J., Duffy J., and Freund, L.B., "The Determination of Dynamic Fracture Toughness of AISI 4340 Steel by the Shadow Spot Method", *J. Mech. Phys. Solids*, **32**, pp. 443-460, 1984.
- [11] Kalthof, J.F., "Shadow Optical Method of Caustics", *Handbook on Experimental Mechanics*, Prentice Hall, 1987, Chapter 9.
- [12] Kishida, K., Yokoyama T., and Nakano, M., "Measurement of Dynamic Fracture Toughness Based on the Split Hopkinson Bar Technique", *Inst. Phys. Conf. Ser. No. 70*, pp. 221-228, 1984.

- [13] Yokoyama T., and Kishida, K., "Measurement of Dynamic Fracture Initiation Toughness By a Novel Impact Three-Point Bend Test Technique Using Hopkinson Pressure Bars", Impact Loading and Dynamic Behaviour of Materials Conference, Bremen, 1987.
- [14] Epstein, J.S., Deason, V.A., and Reuter, W.G., "Dynamic Moire Interferometry Studies of Stress Wave/Crack tip Diffraction Events in 4340 Steels", Draft of paper presented at 19th Symposium on Fracture Mechanics, 1986.
- [15] Crostack, H.A., Krüger, A., "Measuring Dynamic Stress Distributions by Laser Speckle Techniques", Impact Loading and Dynamic Behaviour of Materials Conference, Bremen, 1987.
- [16] Demler, T., Klenk, A., "Basic Research on the Near-Field of Dynamically Loaded Crack Tips", Impact Loading and Dynamic Behaviour of Materials Conference, Bremen, 1987.
- [17] Novinbakht, J., "Determination of Dynamic Stress Intensity Factor ( $K_I^{dyn}$ ) Using Computer Vision", Ph.D. Thesis, University of South Carolina, 1981.
- [18] Freund, L.B., "Crack Propagation in an Elastic Solid Subjected to General Loading. I. Constant Rate of Extension", *J. Mech. Phys. Solids* **20** pp. 129-140 (1972).
- [19] Freund, L.B., "Crack Propagation in an Elastic Solid Subjected to General Loading. II. Nonuniform Rate of Extension", *J. Mech. Phys. Solids* **20** pp. 141-152 (1972).
- [20] Freund, L.B. and Clifton, R.J., "On the Uniqueness of Elastodynamic Solutions for Running Cracks", *J. Elasticity* **4** pp. 293-299 (1974).
- [21] Achenbach, J.D., "Crack Propagation Generated by a Horizontally Polarized Shear Wave", *J. Mech. Phys. Solids* **18** pp. 245-259 (1970).
- [22] Knauss, W.G. and Ravi-Chandar, K., "Fundamental Considerations in Dynamic Fracture", *Engineering Fracture Mechanics* **23** pp. 9-20 (1986).
- [23] Kanninen, M.F., Ahmad, J. and Barnes, C.R., "Dynamic Elastic-Plastic Analysis of Rapid Crack Propagation", *Workshop on Dynamic Fracture*, California Institute of Technology, pp. 226-233 (1983).
- [24] Hutchinson, J.W., "Singular Behavior at the End of a Tensile Crack in a Hardening Material", *J. Mech. Phys. Solids* **16** pp. 13-32 (1968).
- [25] Rice, J.R. and Rosengren, G.F., "Plane Strain Deformation Near a Crack Tip in a Power-Law Hardening Material", *J. Mech. Phys. Solids* **16** pp. 1-12 (1968).
- [26] Kanninen, M.F. and Popelar, K.H., *Advanced Fracture Mechanics*, Oxford (1985).

- [27] Rice, J.R., "Mathematical Analysis in the Mechanics of Fracture", in *Fracture Vol. II* (H. Liebowitz, ed.), Academic Press, pp. 191-311 (1968).
- [28] Chitaley, A.D. And McClintock, F.A., "Elastic-plastic Mechanics of Steady Crack Growth under Antiplane Conditions", *J. Mech. Phys. Solids* **19** pp. 147-163 (1971).
- [29] Slepyan, L.I., "Crack Dynamic in an Elastic-Plastic Body", *Mekhanika Tverdogo Tela* (English Translation) **11** pp. 126-134 (1976).
- [30] Dunayevsky, V. and Achenbach, J.D., "Boundary Layer Phenomenon in the Plastic Zone Near a Rapidly Propagating Crack Tip", *Int. J. Solids and Structures* **18** pp. 1-12 (1982).
- [31] Gao, Y.C. and Nemat-Nasser, S., "Dynamic Fields Near a Crack Tip Growing in an Elastic-Perfectly Plastic Solid", *Mechanics of Materials* **2** pp. 47-60 (1983).
- [32] Hui, C.-Y. and Riedel, H., "The Asymptotic Stress and Strain Field Near the Tip of a Growing Crack Under Creep Conditions", *Int. J. Fracture* **17** pp. 409-420 (1981).
- [33] Lo, K.K., "Dynamic Crack-tip Fields in Rate Sensitive Solids", *J. Mech. Phys. Solids* **31** pp. 287-305 (1983).
- [34] Freund, L.B. and Douglas, A.S., "The Influence of Inertia on Elastic-Plastic Antiplane Shear Crack Growth", *J. Mech. Phys. Solids* **30** pp. 59-74 (1982).
- [35] McClintock, F.A. and Irwin, G.R., "Plasticity Aspects of Fracture Mechanics", in *Fracture Toughness Testing and Its Applications*, *ASTM STP 381* pp. 84-113 (1965).
- [36] Freund, L.B. and Douglas, A.S., "Dynamic Growth of an Antiplane Shear Crack in a Rate Sensitive Elastic-Plastic Material", in *Elastic-Plastic Fracture - Vol. I ASTM STP 803*, (Shih, C.F. and Gudas, J. eds.), pp. 5-20, American Society for Testing and Materials, Philadelphia (1983).
- [37] Lam, P.S. and Freund, L.B., "Analysis of Dynamic Growth of a Tensile Crack in an Elastic-Plastic Material", *J. Mech. Phys. Solids* **33** pp. 153-167 (1985).
- [38] Freund, L. B., Hutchinson, J. W. and Lam, P. S., "Analysis of High-strain-rate Elastic-plastic Crack Growth", *Engineering Fracture Mechanics* **23** pp. 119-130 (1986).
- [39] Brickstad, B. and Nilsson, F., "Dynamic Analysis of Crack Growth and Arrest in a Pressure Vessel Subjected to Thermal and Pressure Loading", *Engineering Fracture Mechanics* **23** pp. 61-70 (1986).

- [40] Homma, H., Shockey, D. A. and Murayama, Y., "Response of Cracks in Structural Materials to Short Pulse Loads", *J. Mech. Phys. Solids* **31** pp. 261-279 (1983).
- [41] Shockey, D.A., Erlich, D.C., Kalthoff, J.F. and Homma, H., "Short-pulse Fracture Mechanics", *Engineering Fracture Mechanics* **23** pp. 311-319 (1986).
- [42] Homma, H., Shockey, D.A. and Hada, S., "Minimum Time Criterion for Crack Instability in Structural Metals", in *Fracture Mechanics: 17th Volume, ASTM STP 905*, (Underwood, J.H. et al. eds.) pp. 683-696, American Society for Testing and Materials, Philadelphia (1986).
- [43] Costin, L.S., Duffy J. and Freund L.B., "Fracture Initiation in Metals Under Stress Wave Loading Conditions", in *Fast Fracture and Crack Arrest, ASTM STP 627* (Hahn, G.T. and Kanninen, M.F., eds.), pp. 301-318. American Society for Testing and Materials, Philadelphia (1977).
- [44] Wilson M.L., Hawley R.H. and Duffy J., "The Effect of Loading Rate and Temperature on Fracture Initiation in 1020 Hot-Rolled Steel", *Engng Fracture Mech.* **13**, 371-385 (1980).
- [45] Nakamura, T., Shih, C.F. and Freund, L.B., "Elastic-plastic Analysis of a Dynamically Loaded Circumferentially Notched Round Bar", *Engineering Fracture Mechanics* **22** pp. 437-452 (1985).
- [46] Nakamura, T., Shih, C.F. and Freund, L.B., "Computational Methods Based on an Energy Integral in Dynamic Fracture", *Int. J. Fracture* **27** pp. 229-243 (1985).
- [47] Rice, J.R., Paris, P.C. and Merkle, J.G., "Some further Results of *J*-integral Analysis and Estimates", in *Progress in Flaw Growth and Fracture Toughness Testing, ASTM STP 536* pp. 231-245 (1973).
- [48] Nakamura, T., Shih, C.F. and Freund, L.B., "Analysis of a Dynamically Loaded Three-point-bend Ductile Fracture Specimen", *Engineering Fracture Mechanics* **25** pp. 323-339 (1986).
- [49] Nakamura, T., Shih, C.F. and Freund, L.B., "Three-dimensional Transient Analysis of a Dynamically Loaded Three-point-bend Ductile Fracture Specimen", *Brown University Report ONR0365/3* (1986).
- [50] Newman, J.C., Booth, B.C. and Shivakumar, K.N., "An Elastic-Plastic Analysis of the *J*-Resistance Curve Using a CTOD Criterion", ASTM Proceedings of the Eighteenth National Symposium on Fracture Mechanics, (1985).
- [51] Zikry, M., "A Three Dimensional Finite Element Analysis of Crack Growth for Aluminum CS-19", M.S. Thesis *The Johns Hopkins University* (1986).

- [52] Rosakis, A.J. and Ravi-Chandar, K., "On Crack Tip Stress State: an Experimental Evaluation of Three Dimensional Effects", *Int. J. Solids Structures* **22** pp. 121-134 (1986).
- [53] Akin, J.E., *Application and Implementation of Finite Element Methods*, Academic Press, New York (1982).
- [54] Cowper, G. R. and Symonds, P. S., "Strain Hardening and Strain-Rate Effects in the Impact Loading of Cantilever Beams", Technical Report No. 28, Brown University, September 1957.
- [55] Perzyna, P., "Fundamental Problems in Viscoplasticity", *Advances in Applied Mechanics*, **9**, Academic Press, New York (1966).
- [56] Rice, J.R., "On the Structure of Stress-Strain Relations for Time-Dependent Plastic Deformation in Metals", *J. Appl. Mech.*, **37**, pp. 728-737 (1970).
- [57] Kendall, D. P., "The Effect of Strain Rate and Temperature on Yielding in Steels", *J. Basic Eng. (Transactions ASME)*, **94**, pp. 207-212 (1972).
- [58] Lindholm, U. S. and Johnson, G. R., "Strain-Rate Effects in Metals at Large Shears", in *Material Behavior Under High Stress and Ultrahigh Loading Rates*, (Mescall, J. and Weiss, V. eds.), pp. 61-79, Plenum Press, New York (1983).
- [59] Tanimura, S. and Duffy, J., "Strain Rate Effects and Temperature History Effects for Three Different Tempers of 4340 VAR Steel", *Int. J. Plasticity*, **2**, pp. 21-35 (1984).
- [60] Jones, N., "Structural Aspects of Ship Collisions", in *Structural Crashworthiness*, (Jones, N. and Wierzbicki, T., eds.), pp. 308-337, Butterworths, London (1983).
- [61] Hilber, H.M., Hughes T.J.R. and Taylor, R.L. "Improved Numerical Dissipation of Time Integration Algorithms in Structural Dynamics" *Earthquake Engineering and Structural Dynamics* **5**, pp. 283-292 (1977).
- [62] Hibbitt, H.D. "Some Follower Forces and Load Stiffness" *Int. J. Num. Meth. Eng.* **14**, pp. 937-941 (1979).
- [63] Belytschko, T. "A Survey of Numerical Methods and Computer Programs for Dynamic Structural Analysis" *Nuc. Eng. and Design* **37**, pp. 23-34 (1976).
- [64] Jenkins, F.A. and White, H.E., *Fundamentals of Optics*, McGraw-Hill, 1957.
- [65] Sharpe, W. N., Jr., "Applications of the Interferometric Strain/Displacement Gage", *Optical Engineering*, **21**, pp. 483-488, 1982.

- [66] Sharpe, W.N., Jr., "Dynamic Strain Measurement with the Interferometric Strain Gage", *Experimental Mechanics*, **10**, pp. 89-92, 1970.
- [67] Sharpe, W.N., Jr. and Ward, M., "Benchmark Cyclic Plastic Notch Strain Measurements", *J. of Engineering Materials and Technology*, **105**, pp. 235-241, 1983.
- [68] Zehnder, A.T. and Rosakis, A.J., "Dynamic Fracture Initiation and Propagation in 4340 Steel under Impact Loading", SM Report 86-6, California Institute of Technology, 1986.
- [69] Couque, H., Asaro, R.J., Duffy, J., and Lee, S.H., "Correlations of Microstructure with Dynamic and Quasi-Static Fracture in a Plain Carbon Steel", Division of Engineering, Brown University, 1987.



## A Finite Element Computational Details

This appendix outlines the computational procedures used in simulating the static and dynamic fracture initiation experiments. Since there are four materials, each of which was tested statically and dynamically, a number of computations were performed to simulate these experiments. However, results are presented only for the tool steel (SAE-O1) and 4340 steel. These two materials represent the extremes of material rate sensitivity and dynamic fracture toughness elevation. These calculations therefore provide the reader with sufficient information about both the details of the computational procedures used and the validity and interpretation of the results.

Since the crack initiation toughness is of primary interest here, all experimental simulations were done for a stationary crack. The crack is not advanced and therefore no crack growth law is required. However, the release of several nodes was attempted to simulate the experiments and obtain full-field information for the static analysis of 4340 steel specimen. The crack is assumed to be mathematically sharp and the effects of closure due to the fatigue procedure for obtaining a sharp crack, are ignored. It is assumed that the deformation is small, that the material is isotropic and homogeneous and that elastic and plastic strain additively decompose.

### A.1 General Modeling Procedures

#### A.1.1 Mesh Details

Static calculations require a modeling of the specimen only, while the dynamic simulation necessitates the modeling of the projectile (with an initial velocity), tup and specimen. Since the fatigue precracking procedure produces initial crack lengths which are not completely uniform, each mesh (i.e. for both the static and the dynamic calculations) is adjusted to produce a crack of the correct length.

In the *static* test simulations, the specimen is modeled by two-dimensional plane stress and plane strain elements. Most of the specimen is comprised of plane stress elements, while a small area near the crack tip (the radius of this region is about 10%-30% of the specimen thickness) is modeled using plane strain elements. This combination of plane stress and plane strain deformation effectively allows a 2-D calculation to simulate 3-D effects—with the accompanying economy in the calculations—and has been used to good effect before by Newman [50,51] and corresponds reasonably with the experimental evidence reported by Rosakis and Ravi-Chandar [52]. Two eight-node plane strain isoparametric elements with the mid-side nodes placed at the quarter points closest to the crack tip are used around the crack tip. This technique effectively simulates the elastic singularity for purely elastic deformation [53].

The graded specimen mesh (see Figures 51 and 52) used in the static calculations has four-node quadrilateral finite elements in combination with 18 eight-node elements

surrounding the crack tip. Full integration is used for the four-node elements and reduced integration for the eight-node elements. Eight-node elements is on the order of  $35\text{ }\mu\text{m}$  by  $50\text{ }\mu\text{m}$  in the neighborhood of the crack. The motion of the node  $35\text{ }\mu\text{m}$  from the crack flank and  $100\text{ }\mu\text{m}$  behind the crack simulates the indent motion. In the remote regions the elements are on the order of  $1\text{ mm}$  in size. This gives a mesh with 178 elements and 546 degrees of freedom. Only the one half of specimen itself need be modeled due to symmetry.

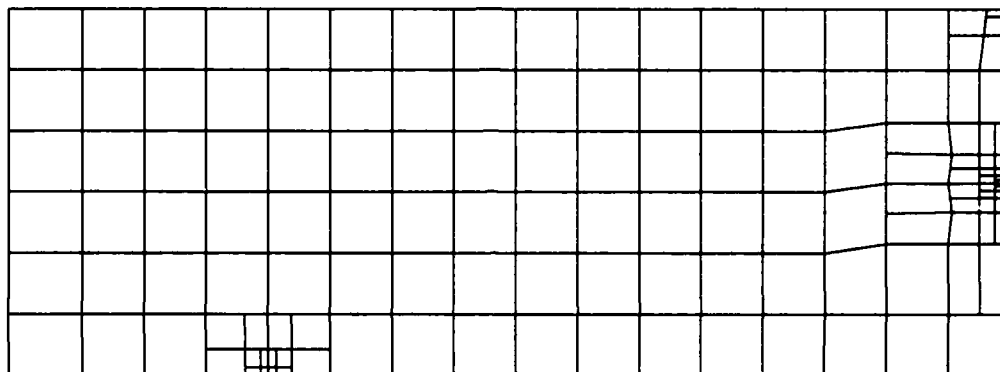


Figure 51: Graded Finite Element Mesh Used in Static Calculations

*Dynamic* simulation is more complex and requires that all the interacting components of the system be modeled. Therefore, the specimen, tup and projectile must all be included in the finite element model (see Figure 53). The tup is modeled by 40 four-node plane strain elements (54 nodes) and the projectile by 54 four-node plane strain elements (77 nodes). In the graded mesh dynamic model the total number of finite elements is 273 resulting in a 792 degree of freedom model.

In the dynamic tests, inertia plays a major role, and the combination of plane stress and plane strain elements may lead to undesirable stress wave reflections and impedance mismatch at the plane stress/plane strain interface. To check the effect of spurious wave reflections at element boundaries and impedance mismatch caused by a steeply graded mesh model for specimen on the dynamic response, a uniform mesh model (see Figure 54) was also used in the dynamic calculations. This model has the same tup and

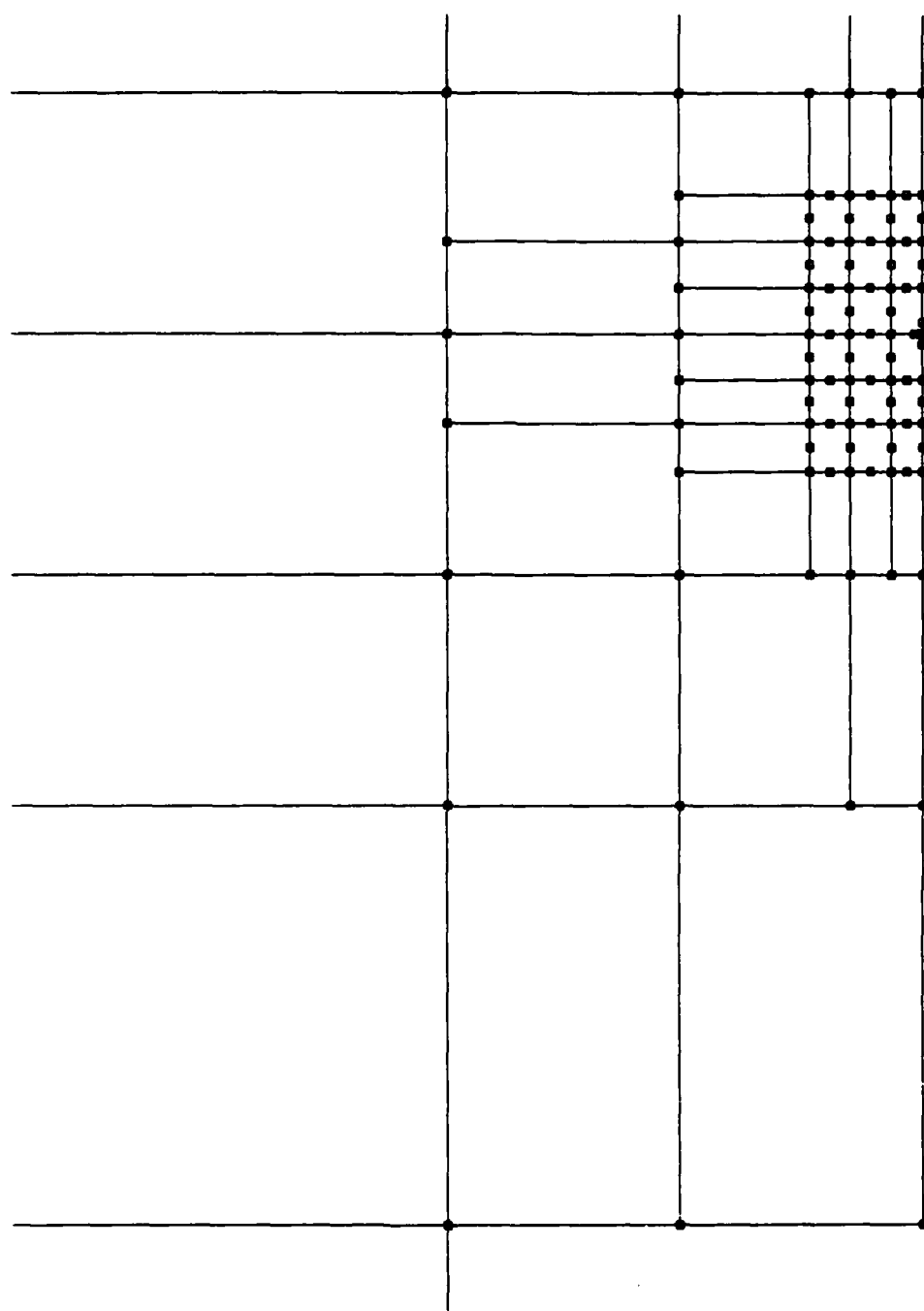


Figure 52: Near-tip Detail of Graded Mesh Used in Both Static and Dynamic Calculations

projectile as the graded mesh model, but the specimen with uniform meshes consists of 84 plane strain 8 noded elements of approximately 1 mm on a side. This results in a uniform mesh model for dynamic simulation with 283 nodes and 808 degrees of freedom for the entire system.

### A.1.2 Time Integration

Dynamic calculations were performed using the Hilber-Hughes-Taylor (HHT) [61] implicit time integration algorithm, with a fixed time step. Since the implicit integration scheme is stable, this allows for larger time increments. Equilibrium tolerance (parameter PTOL) is required for implicit integration. All forces at all nodes must fall below this tolerance for the solution to be accepted. Usually PTOL is set to a small fraction ( $10^{-2}$  to  $10^{-4}$ ) of typical actual force values. A small amount of damping is provided for by setting the HHT parameter  $\alpha = -0.05$  which removes the high frequency oscillations. An examination of the energy balance shows that this damping does not cause more than an insignificant amount of dissipation. For a discussion of implicit time integration schemes for the impact response of structures, see Belytschko [63].

The dynamic graded mesh calculation required approximately 3.5 CPU hours on a MicroVAXII or 9 CPU minutes on a CRAY to simulate the first 15  $\mu$ s of the impact fracture test.

### A.1.3 Materials Response

The *quasi-static* material stress versus strain laws, as given in Section 4, are modeled as isotropic hardening, multi-linear, elasto-plastic materials using a von Mises yield criterion. The engineering 0.2% offset stress is not used as the yield stress—the onset of plasticity is taken to occur at the end of the linear region of the stress versus strain curve, see Figure 3.

The *dynamic* constitutive behaviour of materials is very complicated and only very restricted amount of data is available for some materials. However, viscoplastic effects are very important in these calculations and a flow-stress versus stain-rate material law of the type [54,55,56]

$$\dot{\epsilon}^p = D (\sigma/\sigma_0 - 1)^P \quad \text{for} \quad \sigma \geq \sigma_0 \quad (\text{A.1})$$

is used for the dynamic calculations. Here,  $\sigma$  is the effective yield stress at a nonzero strain rate,  $\sigma_0$  is the static yield stress (which may depend on the equivalent plastic strain,  $\epsilon^p$ , via isotropic hardening), and  $\dot{\epsilon}^p$  is the plastic strain rate. The variation of von Mises stress  $\sigma$  versus plastic strain rate  $\dot{\epsilon}^p$  for tool steel and 4340 steel are shown in Figure 55. The choice of the material parameters  $D$  and  $P$  was made after an review of high strain-rate testing, including [57,58,59,60].

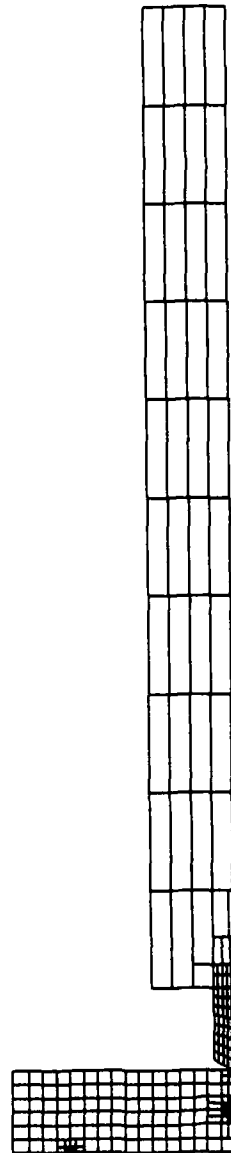


Figure 53: Graded Mesh with Tup and Projectile Used for Dynamic Calculations

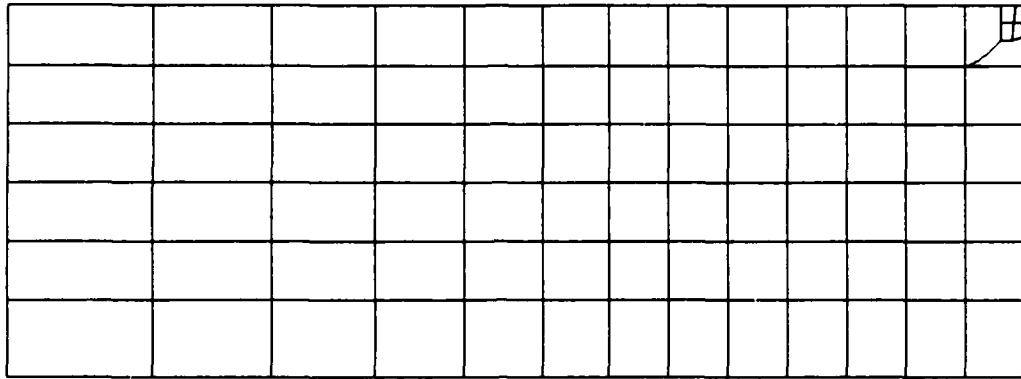


Figure 54: Uniform Mesh Used in Dynamic Calculations

#### A.1.4 Impact

The impact of the projectile (which has a mass greater than 5 times the mass of the tup and specimen combined) with the tup and specimen is modeled by giving the projectile the experimentally measured velocity for that experiment. Tup and specimen begin with zero velocity. Impact is assumed to be perfect and normal.

The crack initiation process is completed in less than 20  $\mu\text{s}$  and the deformation is therefore considered to be adiabatic. Since our main concern is the displacement field near the crack tip in the first 10 to 20  $\mu\text{s}$ , the friction between the specimen and the tup and the specimen and the supports is ignored.

### A.2 Results of Static Calculations

#### A.2.1 Tool Steel

In a two-dimensional finite element simulation of fracture experiments, the size of the plane strain dominated region will vary depending on the characteristics of the material and of the specimen. The combination of a plane stress model with plane strain elements cannot represent completely the complicated and three-dimensional fracture processes. The size of plane strain region will affect the elastic stiffness of the model, and larger

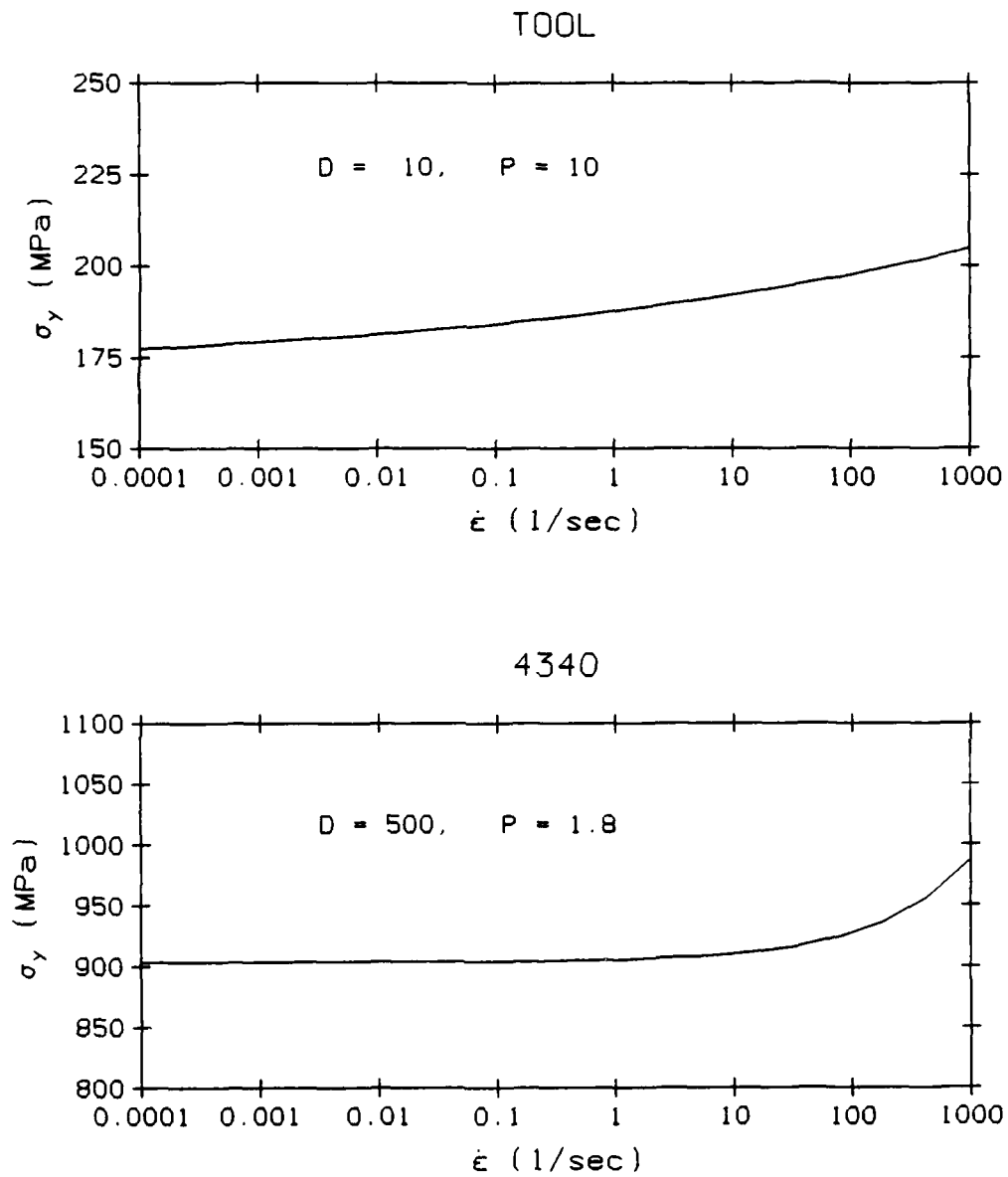


Figure 55: Von Mises stress  $\sigma$  vs. plastic strain rate  $\dot{\epsilon}^p$  for tool steel and 4340 steel.

plane strain region the stiffer the response. The elastic region (which is not the region of most interest here) is therefore used to "calibrate" the model, viz. to choose the size of the plane strain region.

The size of the plane strain region around the crack tip is 2.12 mm by 4.23 mm. This region corresponds to one third of the specimen thickness, i.e. 2.13 mm (thickness of the specimen is 6.4 mm). The adjusted initial crack length is 6.787 mm with the crack tip located at  $x = 0.0$  mm and  $y = 0.437$  mm from the origin of the finite element meshing coordinates. The ligament of this specimen is 5.913 mm.

Since only the half of a specimen is considered due to symmetry, the load applied to the finite element model is the half of the actual applied load with the increment of 56 N in each loading step and the maximum load of 2800 N. The coefficient of tolerance (PTOL in ABAQUS) used in the calculation is 1 N. The given load increment and the coefficient of tolerance provide convergent solution up to 2800 N, which sufficiently covers the loading range of the experiments.

The CTOD by finite element simulation gives good agreement with experimental data for the most loading process except at the initial loading stage where the specimen must overcome the closure load as shown in 56.

The calculated CMOD curve lies between envelopes of the measured CMOD curve from the clip gage until the calculated curve starts to deviate from envelopes under the load larger than 2200 N, 57. The calculated curve is more convex than the measured one. That makes the critical fracture load ( $P_q = 1161$  N) based on finite element simulation 40% lower than that ( $P_q = 2046$  N) based on experiments.

#### A.2.2 4340 Steel

The size of the plane strain region for 4340 steel is 0.2709 mm by 0.5418 mm. This region is therefore a sub-set of the area around the crack tip with a radius equal one third of the specimen thickness. The crack length is 6.646 mm with the crack tip located at  $x = 0.0$  mm and  $y = 0.296$  mm from the origin of the finite element coordinates. The ligament of this specimen is 6.054 mm.

The use of non-singular elements around the crack tip was found to be of little significance, and allowed crack growth to take place by the simple nodal-release technique. Each opening of the crack tip corresponds to a crack growth of 0.026 mm, and a total crack growth of 0.104 mm (or 1.6% crack growth) is required to simulate the pre-initiation fracture process.

The small crack growth simulation (Figure 58) gives finite element results conforming to the experimental data except at the initial loading stage where the specimen must overcome the closure load. The finite element CMOD calculations also show good agreement with the experimental data. Determination of the critical fracture load,  $P_q$ ,



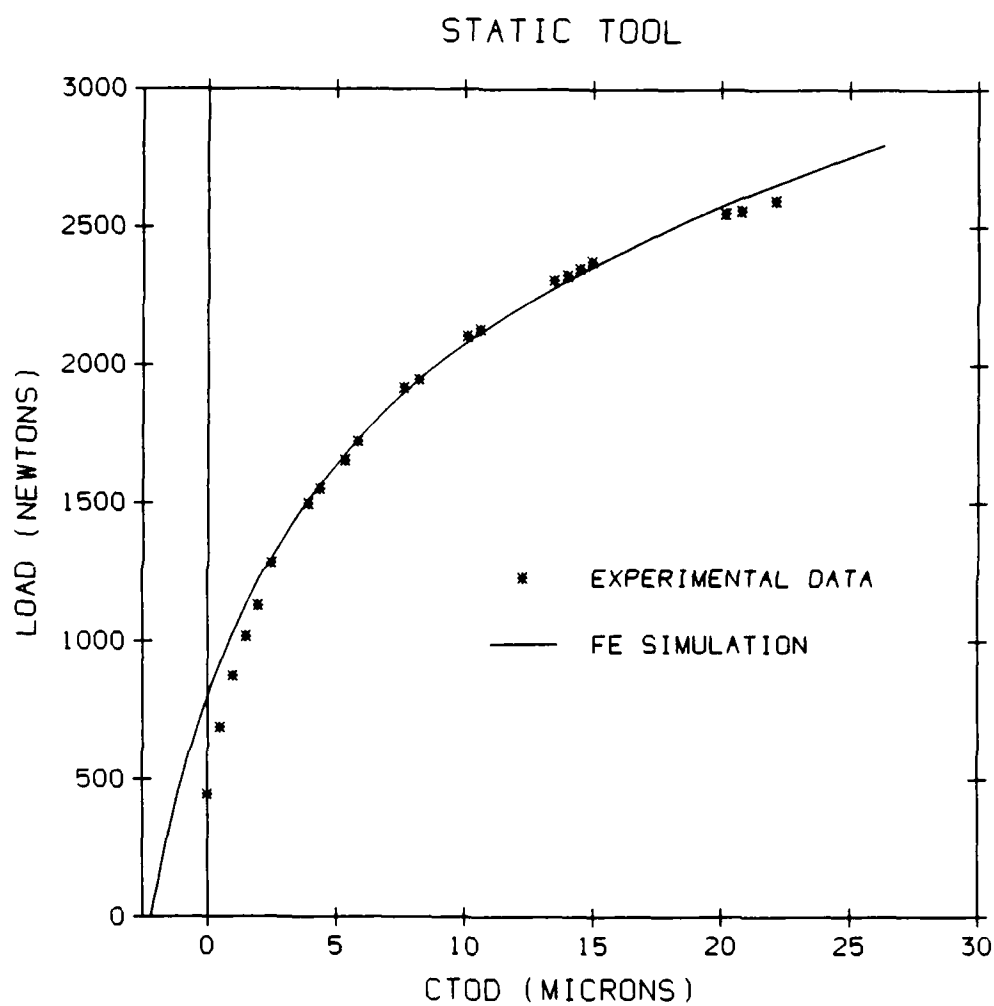


Figure 56: CTOD vs. Load for Tool Steel in Static Calculations

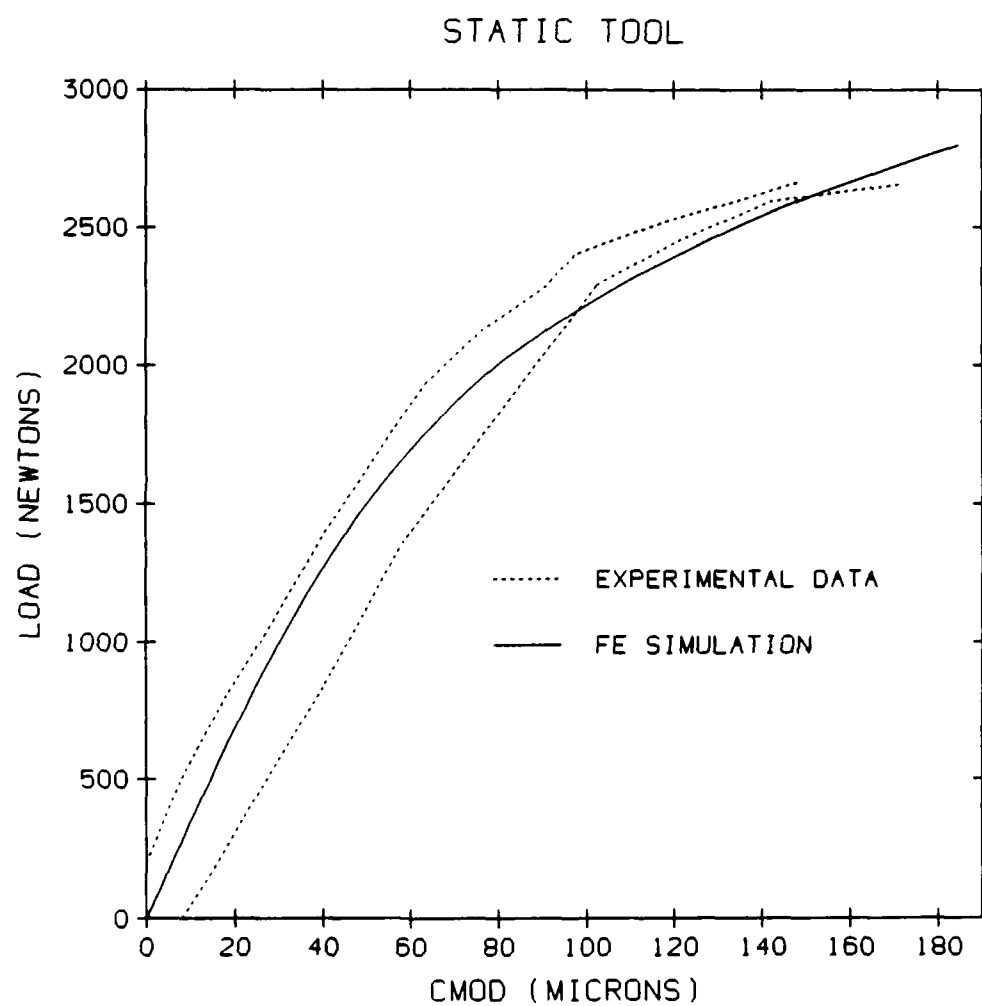


Figure 57: CMOD vs. Load for Tool Steel in Static Calculations

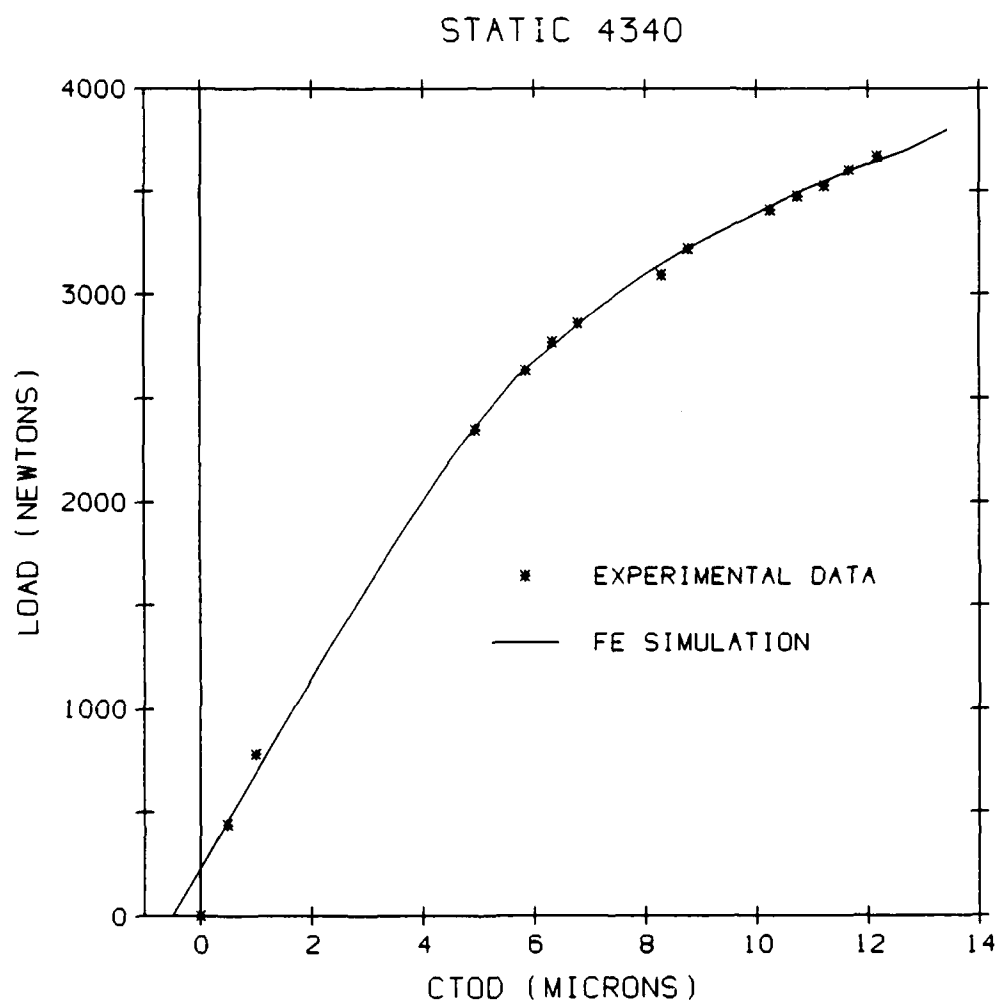


Figure 58: CTOD vs. Load for 4340 Steel in Static Calculations

based on finite element results give  $P_q = 3525$  N. This is only about 3% less than the critical load obtained by experiment; experimental  $P_q = 3636$  N, see Figure 59).

CTOD measurement is more sensitive than CMOD in detecting when crack start propagating. The determination of critical fracture load based on experimental CMOD, in this case, gives the critical load where the crack has already propagated about 0.100 mm. This information is based on finite element analysis only, since the specimen can no longer be used to verify this result.

From the finite element results the following interesting observation can be made. At the load levels at which the nodes are released, the von Mises effective stresses just ahead of the crack tip reach their maximum value. This suggest a stress controlled crack growth behavior prior to true (ASTM-E399 defined) initiation.

At the critical fracture load (based on CMOD measurements), finite element analysis shows that the crack has already propagated to less than 2% of the initial precrack length. However, this cannot be verified by experimental data because the specimen is loaded until total failure takes place. An experiment aided by finite element analysis may be performed to obtain critical fracture load without destroying the specimen, hence crack growth can be measured. To detect the initiation of crack growth, being immediately around the crack tip, CTOD measurement is more accurate and sensitive than the CMOD. This is shown by both experimental and finite element results. Therefore the present ISDG (Interferometric Strain/Displacement Gage) technique is recommended for obtaining more precise fracture information near the crack tip.

### A.3 Results of Dynamic Calculations

#### A.3.1 Tool Steel

The finite element model for dynamic analysis includes the tool steel tup and the aluminium projectile in addition to tool steel specimen. The adjusted initial crack length is 6.731 mm with the crack tip located at  $x = 0.0$  mm and  $y = 0.381$  mm from the origin of the finite element meshing coordinates. The ligament of this specimen is 5.969 mm. The projectile hits the tup and specimen with the initial velocity of 35.278 m/s and the loading rate is 241.35 N/s. The viscoplastic effect of material response is considered in the computation due to high loading rate. The contact time of 15 micro-seconds is considered in the finite element computations. The tolerance parameter PTOL used in the calculation is 100 N.

Though the calculated tool steel CTOD vs. time curve in Figure 60 shows slightly fluctuating behavior, the agreement is generally good compared with experimental data, except the initial loading stage owing to the closure load effect. However, the finite element results diverge from the experimental observations earlier than the initiation point as defined by the offset technique outlined in Section 9.

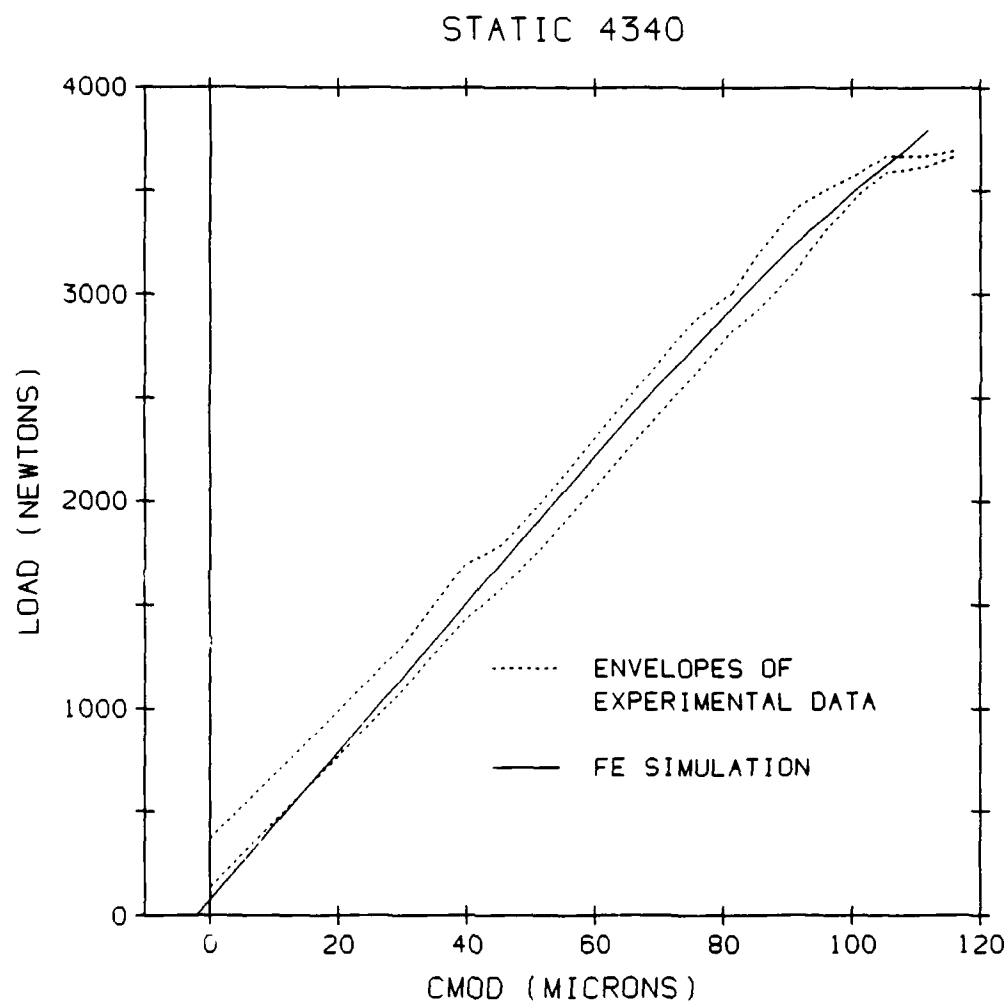


Figure 59: CMOD vs. Load for 4340 Steel in Static Calculations

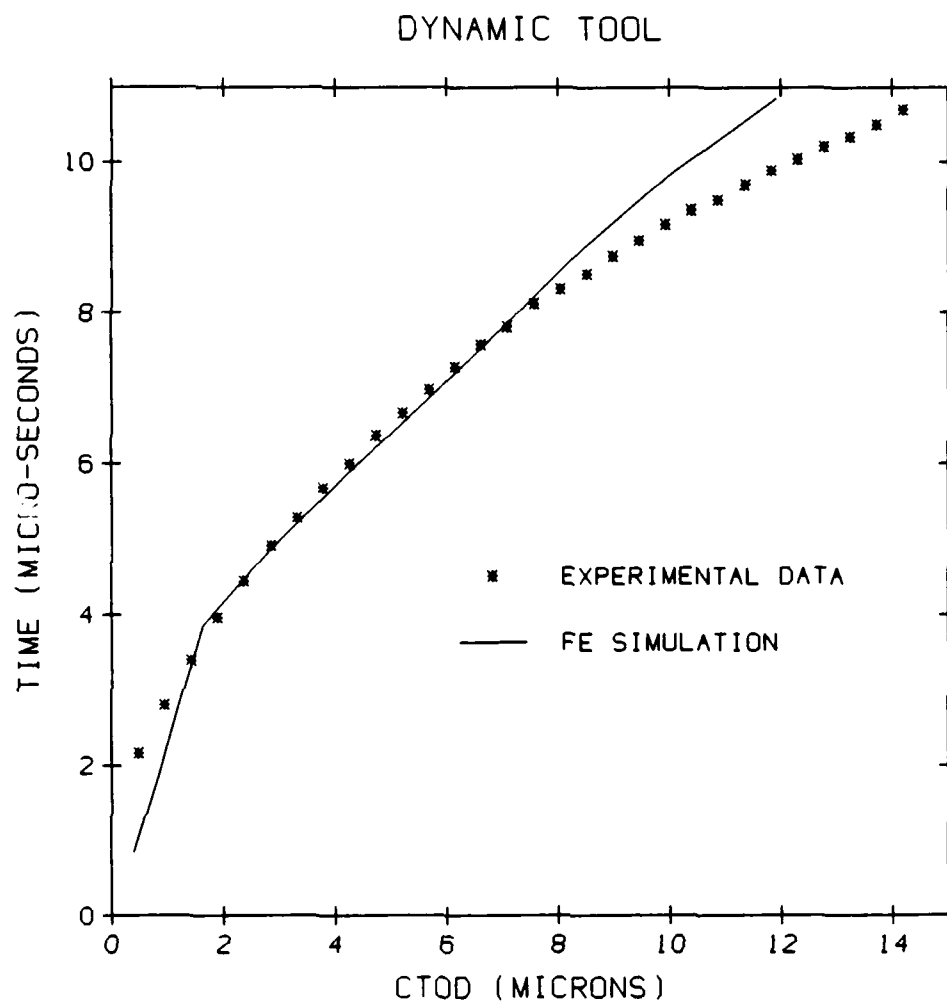


Figure 60: CTOD vs. Time for Tool Steel in Dynamic Calculations

### A.3.2 4340 Steel

Finite element model for dynamic analysis includes the tool steel tup and the aluminium projectile in addition to 4340 steel specimen. The adjusted initial crack length is 6.553 mm with the crack tip located at  $x = 0.0$  mm and  $y = 0.203$  mm from the origin of the finite element meshing coordinates. The ligament of this specimen is 6.147 mm. The projectile hits the tup and specimen with the initial velocity of 43.815 m/s and the loading rate is 385.64 N/s. The viscoplastic effect is considered due to high loading rate. The contact time of 15 micro-seconds is considered in the finite element computations. During the short contact time crack may not have propagated. Hence, there is no need to model crack propagation. The tolerance parameter PTOL used in the calculation is 100 N. The calculated CTOD vs. time curve for 4340 steel (shown in Figure 61) shows good agreement with the experimental data after the initial closure load is overcome. The finite element results diverge earlier than the crack initiation time as defined by the offset technique outlined in Section 9.

### A.4 Post-processing

Some small but efficient programs have been developed for the effective post-processing and subsequent analysis of the dynamic fracture event. These include:

1. Automatic generation of the mesh near the crack tip to take account of the variance of crack length due to small differences in the fatiguing process. Although the variance of crack length due to the fatigue process is small compared to the total specimen, it is large in comparison with the elements near the crack tip and disturbs the distribution of nodes in this region.
2. Automatic conversion of mesh data file for FEPLLOT. A post-processing program reads the ABAQUS mesh data, retrieves the pertinent data and converts this data into a format suitable for use by the local mesh plotting routine FEPLLOT.
3. Post-processing of ABAQUS files. This program accesses the ABAQUS unformatted output file, analyses each record, identifies the record content by the key word on the heading and extracts time, displacements, stresses, strains, etc., according to input selection, and reorganizes them in the format suitable for plotting by XYPLLOT (a local scientific plotting procedure).
4.  $J$ -integral Calculation. This program allows  $J$ -integral evaluation, which is based on the domain integral method (see Nakamura *et al.* [48,49], for static and dynamic fracture with a stationary crack. It uses finite element field information (provided here by ABAQUS) and performs  $J$ -integral computations along a user-specified path.

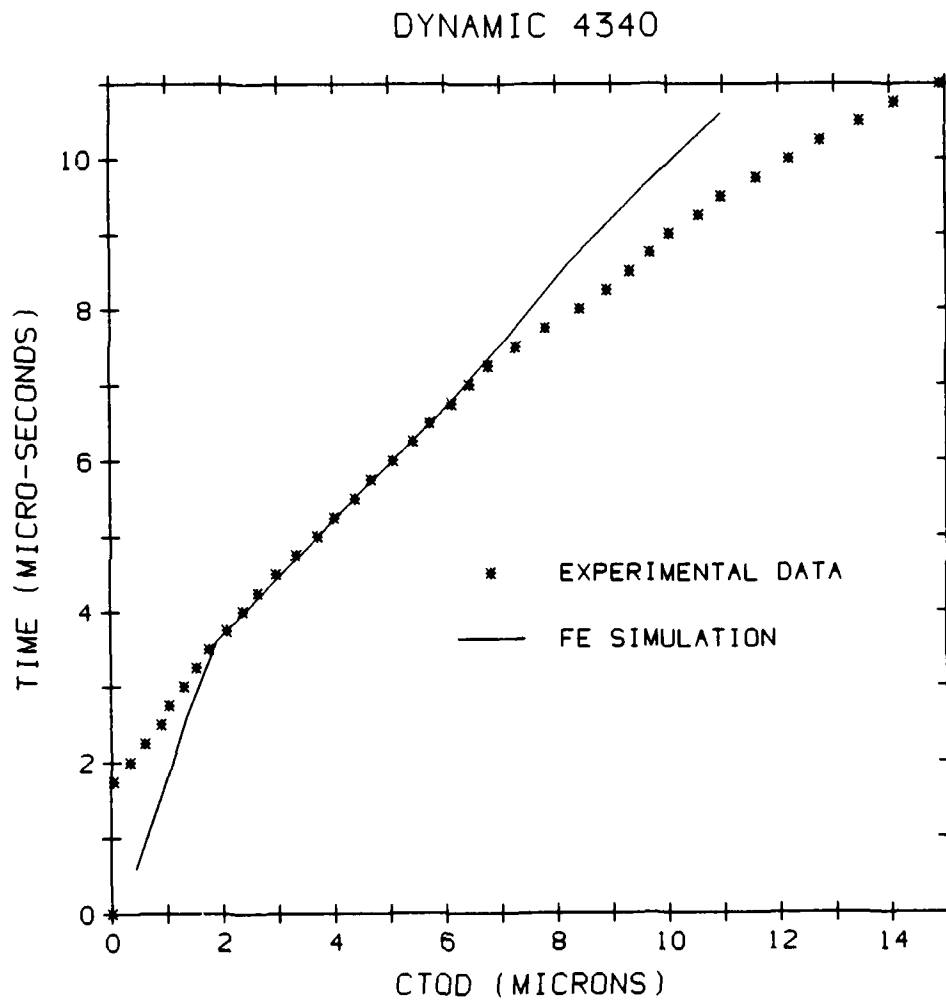


Figure 61: CTOD vs. Time for 4340 Steel in Dynamic Calculations



UNCLASSIFIED

SECURITY CLASSIFICATION OF THIS PAGE (When Data Entered)

REPORT DOCUMENTATION PAGE		READ INSTRUCTIONS BEFORE COMPLETING FORM
1. REPORT NUMBER <b>ARO 22684.2-EG</b>	2. GOVT ACCESSION NO. <b>N/A</b>	3. RECIPIENT'S CATALOG NUMBER <b>N/A</b>
4. TITLE (and Subtitle) <b>Dynamic Fracture Toughness Evaluation by Measurement of CTOD</b>		5. TYPE OF REPORT & PERIOD COVERED <b>Interim Technical</b>
		6. PERFORMING ORG. REPORT NUMBER
7. AUTHOR(s) <b>William N. Sharpe, Jr., Andrew S. Douglas, Jason M. Shapiro</b>		8. CONTRACT OR GRANT NUMBER(s) <b>DAAG29-85-K-0218</b>
9. PERFORMING ORGANIZATION NAME AND ADDRESS <b>Department of Mechanical Engineering The Johns Hopkins University Baltimore, MD 21218</b>		10. PROGRAM ELEMENT, PROJECT, TASK AREA & WORK UNIT NUMBERS
11. CONTROLLING OFFICE NAME AND ADDRESS <b>U. S. Army Research Office Post Office Box 12211 Research Triangle Park, NC 27709</b>		12. REPORT DATE <b>March 15, 1988</b>
		13. NUMBER OF PAGES <b>80</b>
14. MONITORING AGENCY NAME & ADDRESS (if different from Controlling Office)		15. SECURITY CLASS. (of this report) <b>Unclassified</b>
		15a. DECLASSIFICATION/DOWNGRADING SCHEDULE
16. DISTRIBUTION STATEMENT (of this Report)  <b>Approved for public release; distribution unlimited.</b>		
17. DISTRIBUTION STATEMENT (of the abstract entered in Block 20, if different from Report)  <b>NA</b>		
18. SUPPLEMENTARY NOTES  <b>The view, opinions, and/or findings contained in this report are those of the author(s) and should not be construed as an official Department of the Army position, policy, or decision, unless so designated by other documentation.</b>		
19. KEY WORDS (Continue on reverse side if necessary and identify by block number)  <b>Fracture Toughness, Dynamic Testing, Crack Tip Opening Displacement (CTOD), Interferometry, Steel, Tungsten, Dynamic Finite Element Analysis, Rate Sensitivity</b>		
20. ABSTRACT (Continue on reverse side if necessary and identify by block number)  <b>over</b>		

UNCLASSIFIED

SECURITY CLASSIFICATION OF THIS PAGE (When Data Entered)

Quantification of the dynamic fracture toughness of structural materials is essential to a wide range of problems—from nuclear accidents to ordnance applications. However, the difficulties associated with accurate measurements of cracks under dynamic loading are considerable. Thus there are no standardized procedures and few reliable results.

This work describes a systematic study of the dynamic fracture toughness of SAE-01 tool steel, 4340 and HY100 steels and a tungsten, using the ISDG (Interferometric Strain/Displacement Gage) system which has very high frequency resolution. The ISDG system is used to measure the crack tip opening displacement (CTOD) 100 microns behind a fatigue crack tip in a three-point bend specimen subject to a dynamic loading rate on the order of  $1 \times 10^6$  MPa $\sqrt{m}$ /s. Static measurements on similar specimens serve to calibrate the method and ensure consistency with the accepted procedures for static fracture toughness testing (ASTM E-399). Finite element analyses are used to obtain full field information at the point of initiation and to assess the material characteristics which lead to changes in toughness with loading rate.

The major advantage of the method is that information is obtained very close to the crack tip, so that stress wave loading effects are accounted for. A detailed error analysis gives an uncertainty of -10% to +20% in the determination of fracture toughness, which compares with  $\pm 20\%$  for published work.

Results show that 4340 steel, which is strain-rate insensitive, has no significant change in toughness with loading rate. Measurable toughness dependence on loading rate is found for HY-100 and tungsten, which are approximately 15% tougher under dynamic conditions. SAE-01 tool steel shows a significant increase (50%) in fracture toughness for dynamic over static loading.

END

DATE

FILMED

8-88

DTIC